

Reproduction of the charge density wave phase diagram in 1T-TiSe₂ exposes its excitonic character

Chuan Chen,^{1,2} Bahadur Singh,^{1,2} Hsin Lin,³ and Vitor M. Pereira^{1,2,*}

¹Centre for Advanced 2D Materials and Graphene Research Centre,
National University of Singapore, Singapore 117546

²Department of Physics, National University of Singapore, Singapore 117542

³Institute of Physics, Academia Sinica, Taipei 11529, Taiwan

(Dated: December 3, 2018)

Recent experiments suggest that excitonic degrees of freedom play an important role in precipitating the charge density wave (CDW) transition in 1T-TiSe₂. Through systematic calculations of the electronic and phonon spectrum based on density functional perturbation theory, we show that the predicted critical doping of the CDW phase overshoots the experimental value by one order of magnitude. In contrast, an independent self-consistent many-body calculation of the excitonic order parameter and renormalized band structure is able to capture the experimental phase diagram in extremely good qualitative and quantitative agreement. This demonstrates that electron-electron interactions and the excitonic instability arising from direct electron-hole coupling are pivotal to accurately describe the nature of the CDW in this system. This has important implications to understand the emergence of superconductivity within the CDW phase of this and related systems.

The layered structure of metallic transition metal dichalcogenides (TMDs) has long made them archetypes to study the interplay between charge order, lattice instabilities and superconductivity (SC) in both quasi [1–6] and strictly 2D settings [7–11]. One of their common characteristics is that the SC order is stabilized within (sometimes deeply) a charge density wave (CDW) phase and the phase boundary is rather sensitive to the electronic density. 1T-TiSe₂ (TiSe₂, in short) is a particularly noteworthy case and will be our focus. It is a low-density semi-metal that undergoes a transition to a commensurate triple- \mathbf{q} CDW at a relatively high temperature that increases from $T_c \sim 200$ K in bulk [12], to about 240 K in monolayers [7, 13]. The ordering vectors double the unit cell: $\mathbf{Q}_{\text{cdw}} = 0.5(\mathbf{a}^* + \mathbf{b}^* + \mathbf{c}^*) = \Gamma L$ in the bulk [12], and $\mathbf{Q}_{\text{cdw}} = 0.5(\mathbf{a}^* + \mathbf{b}^*) = \Gamma M$ in the monolayer [7, 14]; the other two wave vectors are symmetric counterparts of \mathbf{Q}_{cdw} under C_3 rotations.

With no Fermi surface nesting [15] and a robust periodic lattice distortion (PLD) in tandem with the CDW [12], it is natural to consider the role played by soft phonons arising from a strong and k -textured electron-phonon coupling, similarly to the cases of 2H-NbSe₂ or 2H-TaSe₂ [16–18]. This would find support in density functional theory (DFT) calculations that reveal softening of an acoustic mode at \mathbf{Q}_{cdw} [19–21] in agreement with inelastic scattering experiments [22, 23]. However, despite structural similarities, TiSe₂ is a fundamentally different electronic system where one expects enhanced electronic interactions: The band structure of the normal state has small overlapping electron and hole pockets offset in momentum by precisely \mathbf{Q}_{cdw} [24, 25], which strongly hints at a possible electronic instability of the excitonic type [12, 26]. Despite the long-standing theoretical prediction for the conditions under which an excitonic insulator ground state should emerge [27–29], no

representative system has yet been decisively found.

Recently, inelastic X-ray measurements identified a dispersive electronic mode compatible with the development of an excitonic condensation at T_c [30]. That excitons and interactions can be important has been increasingly better documented by a number of modeling refinements: Cercellier, Monney, *et al.* showed such mechanism alone could account for a number of features observed in the evolution of the ARPES spectrum of undoped TiSe₂ [31–34] through the CDW transition; based on an approximate quasi-1D model, van Wezel *et al.* dis-

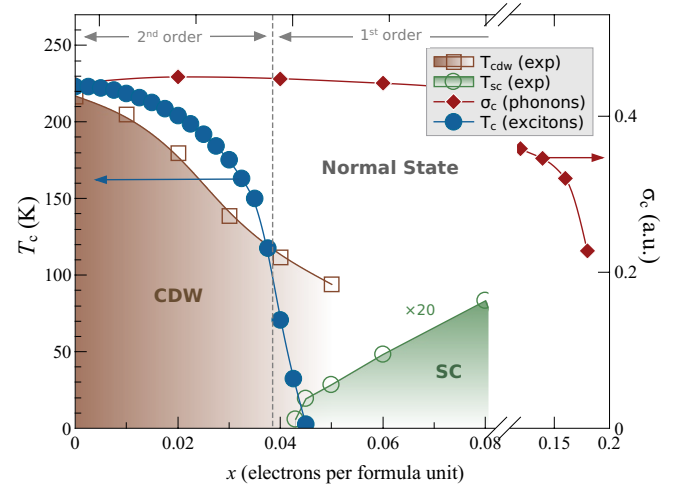


FIG. 1. Filled circles represent $T_c(x)$ obtained from the self-consistent solution of the excitonic instability. The strength of the coupling is the only adjustable parameter, and was fixed at $V = 450$ meV to yield $T_c(0) = 220$ K. The diamonds show the critical smearing parameter (σ_c) above which the phonon instability disappears (note the break in the horizontal axis). Experimental data for T_c (open squares) and T_{sc} (open circles) were extracted from Ref. 5.

covered that exciton condensation can enhance the lattice distortion [35, 36]. Hence, the outstanding question is not whether excitonic physics is at play, but how much so.

Since the dependence of T_c on electronic density is well known experimentally, we submit that the predicted density dependence of T_c in a description with and without account of the excitonic mechanism should be different. As a result, it provides a direct, well defined means to quantify the importance of excitonic condensation in the transition to the CDW phase in TiSe_2 . Indeed, here we demonstrate that the experimental density dependence of T_c in Cu_xTiSe_2 cannot be captured without explicitly accounting for electron-electron interactions and the excitonic instability, as summarized in the calculated phase diagram of Fig. 1.

Excitonic instability—CDW order is stabilized by intra-layer physics (even in bulk TiSe_2 , § S-IV) which explains the strong similarity of electronic and phononic bandstructure changes in monolayer and bulk, as well as their doping phase diagram [5, 9, 13, 37]. Therefore, to interrogate whether the excitonic mechanism is able to drive the system through a CDW transition in agreement with experiments, we study the TiSe_2 monolayer. Although there are two hole pockets [Fig. 3(a)], we consider only the highest one (§ S-I.D), similarly to previous studies [32, 33, 38]. It is modeled as isotropic with $\varepsilon_{v\mathbf{k}} \equiv -\hbar^2\mathbf{k}^2/2m_v + \varepsilon_{bo}$, centered at the Γ point, while the three electron pockets at each M_i point have anisotropic effective masses, $\varepsilon_{c\mathbf{k},i} \equiv \hbar^2(\mathbf{k} - \mathbf{M}_i)_\perp^2/2m_{c,\perp} + \hbar^2(\mathbf{k} - \mathbf{M}_i)_\parallel^2/2m_{c,\parallel}$, as per Fig. 2. When undoped, the chemical potential (μ) of TiSe_2 is placed near the intersection of the conduction and valence pockets, in agreement with the folded DFT band structure calculated in an unrelaxed 2×2 superlattice [cf. Fig. 3(a) later], and also tallying with transport experiments that reveal both electron and hole carriers in the normal state [5, 12]. The band parameters have been extracted by fits to ARPES data in reference 7 in the normal state [39]. Since the bands strongly renormalize near E_F and CDW fluctuations are likely present at $T \gtrsim T_c$ [32], the fitting privileged large energy ranges above and below, rather than the close vicinity of E_F . With these, our normal state electron density is $n_e \sim 4 \times 10^{13} \text{ cm}^{-2}$, consistent with the experimental Hall data [12] (see also Fig. S4).

The Hamiltonian comprises these 4 “bare” bands and a *direct* Coulomb interaction between electrons at the valence and conduction pockets [27–29, 32]:

$$H \equiv \sum_{\mathbf{k},\sigma} \varepsilon_{v\mathbf{k}} c_{\mathbf{k},\sigma}^\dagger c_{\mathbf{k},\sigma} + \sum_{\mathbf{k},\sigma,i} \varepsilon_{c\mathbf{k},i} d_{i,\mathbf{k},\sigma}^\dagger d_{i,\mathbf{k},\sigma} + \frac{1}{\mathcal{N}} \sum_i \sum_{\mathbf{k},\mathbf{k}',\mathbf{q},\sigma,\sigma'} V_{i,\mathbf{q}} c_{\mathbf{k}+\mathbf{q},\sigma}^\dagger d_{i,\mathbf{k}'-\mathbf{q},\sigma'}^\dagger d_{i,\mathbf{k}',\sigma'} c_{\mathbf{k},\sigma}, \quad (1)$$

Here, $c_{\mathbf{k},\sigma}$ ($d_{i,\mathbf{k},\sigma}$) are annihilation operators for electrons

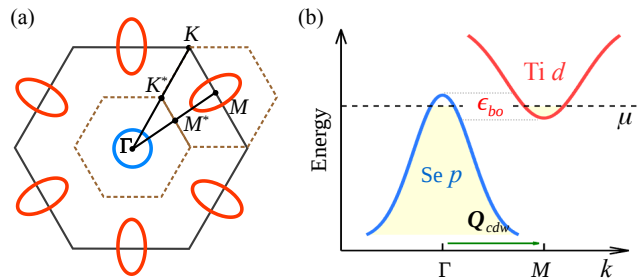


FIG. 2. (a) Schematic of the electron (Γ) and hole (M) pockets in the first Brillouin zone. The dashed lines highlight the folded zones in the 2×2 distorted state. (b) Illustration of the indirect band overlap.

at the valence (i -th conduction) pocket with momentum \mathbf{k} ($\mathbf{M}_i + \mathbf{k}$) and spin σ , and \mathcal{N} is the number of unit cells of the crystal (for electron pockets at \mathbf{M}_i , \mathbf{k} represents the momentum measured from \mathbf{M}_i). The chemical potential μ is implicit in $\varepsilon_{c\mathbf{k}/v\mathbf{k}}$ which are measured with respect to it. A mean-field decoupling generates the order parameter

$$\Delta_{i,\mathbf{k},\sigma}(T) \equiv \frac{1}{\mathcal{N}} \sum_{\mathbf{k}'} V_{i,\mathbf{k}-\mathbf{k}'} \langle d_{i,\mathbf{k}',\sigma}^\dagger c_{\mathbf{k}',\sigma} \rangle \quad (2)$$

that is directly related to the amplitude of the CDW at $\mathbf{k} = \mathbf{Q}_{\text{cdw}}^{(i)}$ [40]. In view of the C_3 symmetry among the three pockets i and the small pocket size, we approximate $V_{i,\mathbf{q}}$ and $\Delta_{i,\mathbf{k},\sigma}$ to i - and \mathbf{k} -independent constants. In particular, $\Delta \equiv \Delta_{i,\mathbf{k},\sigma}$ is the central quantity for our mapping of the temperature-doping phase diagram associated with the excitonic instability. It obeys a self-consistent equation [40], cf. Eq. (S8), whose solution for different μ yields the transition temperature T_c to the CDW phase ($\Delta \neq 0$) as a function of doping.

Self-consistent phase diagram—Fig. 1 shows the resulting T_c , calculated entirely self-consistently at different doping for the first time, and how it compares with the experimental transition temperatures [see also Fig. S2(a)]. It can be clearly seen that: (i) the decreasing trend from $x=0$ follows very well the experimental behavior until $x \approx 0.038$; (ii) the calculation predicts $T_c \rightarrow 0$ at precisely the doping where the CDW changes from commensurate to incommensurate [41] and SC phase emerges ($x \approx 0.04$); (iii) the transition is of 2nd order until $x \approx 0.038$, becoming 1st order afterwards, which correlates with the doping for the onset of discommensurations or ICDW observed in recent experiments [40, 41]. Having set all the bare band parameters from ARPES data as described earlier, *our theory of the charge instability depends only on one parameter*: the coupling V . We set it at 450 meV to match the calculated T_c to the experimental one at $x=0$. With V thus fixed, the results for T_c at different x shown in Fig. 1 follow *without further parameters adjustment*. At $x=0$ we have $\Delta(0) \approx 25 \text{ meV}$

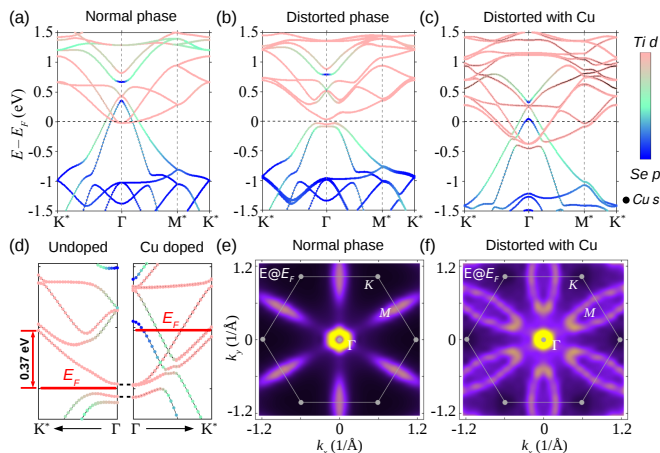


FIG. 3. Band structure obtained with a 2×2 cell in the (a) normal clamped, (b) relaxed distorted (Ti/Se atoms distort by 0.090/0.029 Å), and (c) relaxed configuration with Cu doping. See Fig. S7 for the 1×1 unfolded bands. Panel (d) presents a side-by-side closeup of (b) and (c). (e) and (f) show the energy contours at E_F before and after Cu doping, respectively.

[Fig. S2(b)], in reasonable agreement (given the approximations) with ~ 50 meV measured in bulk and monolayer [7, 38] after subtracting background fluctuations from the latter, as pointed out by Monney *et al.* [31, 38].

Experimental confirmation of whether this mechanism is critical or not in driving the CDW instability in TiSe_2 and related TMDs can be obtained by probing T_c as a function of both electron and hole doping to establish: (i) whether an optimal T_c exists and (ii) whether it correlates with having μ at the pocket intersection.

Note that the absence of nesting implies that the “renormalized” electronic bands in the CDW phase are only partially gapped [32] (Fig. S3). This translates into a predicted increase in the resistivity, $\rho(T)$, as soon as CDW fluctuations set in at $T \gtrsim T_c$, but persistence of the metallic nature at low temperatures; notably, holes are suppressed below T_c . All these features tally with measurements of thermal and electronic transport across the transition [5, 12, 40]. In addition, the preservation of partial electron pockets in the excitonic phase provides a Fermi sea for the development of SC beyond a threshold doping, and the co-existence of SC and CDW order, as seen experimentally [42].

These results reveal that the excitonic mechanism is able to capture correctly all the key qualitative aspects of the CDW transition and, in addition, account quantitatively very well for the experimental doping dependence of T_c . The agreement extends to the position of the CDW critical point that is predicted here to lie rather close to the experimental onset of the SC dome.

Band restructuring ab initio—To obtain an unbiased perspective over the doping dependence of both the reconstructed energy bands and phonon spectrum with

doping, we carried out extensive DFT calculations [43] with the projector augmented wave method implemented in the Vienna Ab-initio Simulation Package (VASP) [44, 45]. Electronic calculations used the generalized gradient approximation (GGA) [46] for the exchange-correlation functional and include spin-orbit coupling. The force constants were obtained within density functional perturbation theory (DFPT) and the phonon dispersions computed with the PHONOPY code [47, 48]. Details of these calculations and methodology are given in the supplementary information [40]. Effect of additional carriers in TiSe_2 were investigated with two complementary strategies: directly simulating supercells with adsorbed Cu and by adding/removing electrons to the unit cell with a neutralizing uniform background charge.

In the high-temperature undistorted phase, TiSe_2 contains two Se p -derived hole pockets at the Γ point slightly overlapping with three Ti d -derived electron pockets at the M point (§ S-I.D.). As these are related by \mathbf{Q}_{cdw} , in a 2×2 superlattice representation they fold to the Γ -point of the reduced Brillouin zone, as explicitly shown in Fig. 3(a). The Fermi energy (E_F) is slightly below the intersection of electron and hole pockets, as required by charge neutrality given the higher number of electron pockets. If one freezes the ions, these bands do not hybridize and revert to their respective primitive BZ positions in the unfolded band structure [cf. Fig. S7(b)].

Relaxing the ions yields a distorted ground-state (the PLD), the overlapping pockets hybridize at E_F , and a gap appears ($E_g = 82$ meV) resulting in an overall lowering of energy. In addition, there is an important restructuring of the bands’ shape near E_F as shown in Fig. 3(b) and Fig. S5; this causes loss of the parabolic dispersion towards an inverted Mexican hat profile. In DFT, this feature was first observed in calculations only after adding GW quasiparticle corrections to the LDA band structure of bulk TiSe_2 [49]. Its observation here at the GGA level indicates it captures the important qualitative details to accurately describe the low density pockets in TiSe_2 (we discuss the electronic structure predicted with an alternative HSE hybrid functional in the supplementary information and Fig. S6). The commensurate 2×2 PLD ground state, the magnitude of the atomic displacements, and nontrivial restructuring of energy bands are in substantial agreement with experiments. The unfolded band structure shown in Fig. S7(d) exhibits distinct back-folded bands at the M point that retain the nontrivial Mexican hat shape, as has been recorded in ARPES [7, 31].

Doping by Cu intercalation—We now add Cu atoms to the monolayer and report in Fig. 3(c) the band structure in the reduced Brillouin zone of a fully optimized 2×2 supercell with two Cu atoms (one above and one below the TiSe_2 slab, to preserve the symmetry). This visibly increases E_F and restores the partial overlap between the electron and hole bands: at this doping, the

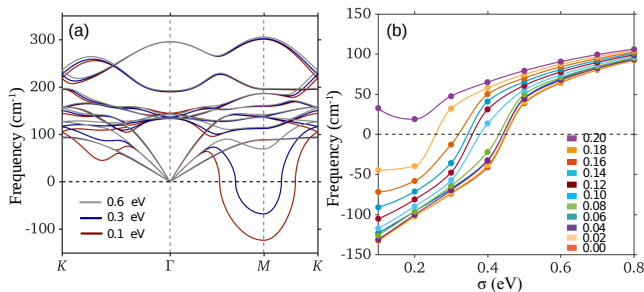


FIG. 4. (a) Phonon spectrum of the 1×1 normal phase with different smearing parameter σ (undoped). (b) Evolution of the soft mode frequency at $\mathbf{k} = M$ as a function of σ (abscissas) and x (legends). Imaginary frequencies are represented as negative values.

system is a semimetal with a rigid upward shift of E_F . This is further evidenced by the Fermi contours shown in Figs. 3(e,f) that shrink at Γ and expand at M to cover a large area of the BZ. Despite having been computed without and with the Cu atoms, these Fermi contours are adiabatically connected, similarly to the evolution of Fermi surfaces in the experiments [50].

There are two crucial effects of doping with Cu. First, inspection of the bands in Figs. 3(b–d) shows that it does not remove the nontrivial restructuring of the dispersion near the electron-hole intersection of the pristine monolayer; Fig. 3(d) emphasizes this observation by placing the undoped and doped band structures near E_F side by side. This agrees with STM measurements showing that the gap in the CDW phase of Cu_xTiSe_2 appears below E_F and moves to higher binding energies proportionally to the Cu content [42]. Second, an analysis of atomic relaxations further reveals that doping nullifies the large atomic displacements observed in the distorted state of the undoped system and entirely suppresses the PLD (Fig. S8).

Note that the concentration of Cu in these supercell calculations is extremely high (Cu:Ti = 50%) for direct experimental comparison (the Cu solubility limit is 11% [5, 51]). The crucial factor here is that, *despite* such high doping, our results provide clear evidence that the leading effect of Cu adsorption is to donate carriers to the conduction bands (one electron per Cu). This rigidly shifts E_F without marked modification of the dispersion and one naturally expects a more dilute scenario to introduce even less perturbation beyond shifting E_F . Therefore, in order to scrutinize in detail the phonon instability at experimentally compatible doping (below 10%), we resort to the second doping strategy mentioned above, which would otherwise require prohibitively large supercells in the DFT and phonon calculations.

Phonon softening ab initio—Fig. 4(a) displays the phonon spectrum of TiSe_2 in the normal (1×1) phase. The qualitative influence of temperature is probed by

varying the electronic smearing parameter σ , which is normally used as a technical tool in the *ab-initio* calculations to accelerate the convergence and, in certain circumstances, acquires the role of electronic temperature [40]. A marked dependence of soft modes on σ is conventionally used to trace *qualitative* changes expected to occur in the real phonon spectrum with temperature. At the smallest smearing ($\sigma = 0.1$ eV), a soft mode with imaginary frequencies (represented as negative values) around the M point signals the dynamical instability towards the 2×2 PLD observed experimentally below T_c , which is complementary to that based on total energy minimization in the 2×2 superlattice discussed above. The fraction of the BZ associated with imaginary frequencies decreases at higher σ and disappears beyond a critical value $\sigma_c \approx 0.45$ eV (note that only one acoustic mode is sensitive to σ , as in experiments [22]). This hardening behavior implies that undoped TiSe_2 should be stable only above a threshold temperature T_c because, while σ_c cannot be directly related to T_c , existence of a finite σ_c can be safely used to predict a finite T_c [40]; this agrees with the experimental situation.

To probe systematically the effect of small uniform doping, we studied the phonon spectrum with different concentrations of electrons in the unit cell (x , measured in electrons per formula unit, FU) as outlined above. The range of imaginary frequencies gradually decreases as x grows, and the soft mode becomes stable above $x_c \sim 0.18$ – 0.20 [cf. Fig. S9(b)]. A summary of the dependence of $\omega(\mathbf{k} = M)$ on both x and σ is shown in Fig. 4(b) for electron doping. A similar progression (not shown) is found with hole doping, albeit with a smaller critical density (~ 0.08 holes/FU). Hence, both electron and hole doping suppress the PLD in a TiSe_2 monolayer.

The variation of σ_c with doping is included in the phase diagram of Fig. 1 for comparison. While our DFPT results correctly predict the suppression of the CDW/PLD in doped TiSe_2 , the rate of suppression with doping is much smaller than in experiments, resulting in an order of magnitude discrepancy between the predicted and experimental x_c . This conclusion is robust with regards to the smearing method used [40].

Discussion—We provided the first complete, self-contained theoretical description of the influence of both temperature and doping in the CDW phase diagram of TiSe_2 in a fully self-consistent way. The solution of the excitonic instability with doping predicts a phase diagram in very good agreement with the experimental $T_c(x)$. This is significant because: our bare band structure is fixed from ARPES data; the single interaction parameter V is fixed once in the undoped case; the good agreement seen for $T_c(x)$ follows without any subsequent parameter fitting. In addition, the electron-phonon coupling can be incorporated straightforwardly in this scheme, possibly enhancing the CDW instability [40, 52].

The commensurate nature of the CDW, where both amplitude and phase fluctuating modes are gapped [53–56], and the high T_c , generically support relying on a mean-field calculation to describe the condensed phase of this problem. However, fluctuations are likely the reason for the persistence of the spectral gap in ARPES even above T_c [7, 31], and for our $\Delta(0) - \Delta(T_c)$ to be 0.5 [Fig. S2(b)] of that same difference in experiments for undoped TiSe_2 [31–33, 38]. The experimental restructuring towards Mexican-hat-shaped bands, with spectral transfer affecting only low energies, indicates that the physics is well described by our mean-field decoupling scheme.

Although DFT+DFPT implementations capture the electron-phonon coupling and some level of electronic correlation, they do not account for the excitonic condensation. By not explicitly capturing this physics, the calculation is unable to describe the correct degree of phonon softening, especially because the very low density places E_F in the region where the spectrum is non-trivially restructured. This sensitivity to electronic interactions tallies with previous evidence that DFT-based results for the stability of the PLD and renormalized band-structure depend strongly on the exchange and correlation functional, the usage of a local or non-local density approximation, and quasiparticle corrections [21, 49, 57–59].

Our results place the excitonic instability as a decisive element in the microscopic description of the CDW/PLD transition, as hinted by recent experiments that unveiled hybridized excitonic and phonon modes [30]. The current ability to map the phase diagram in strictly 2D TiSe_2 by gate doping [9] should allow forthcoming studies of the yet unexplored hole-doped regime, e.g., whether an optimal T_c correlates with E_F at the intersection of the electron and hole pockets, as predicted here.

We thank Lei Su and A. H. Castro Neto for fruitful discussions. VMP was supported by the Singapore Ministry of Education through grant MOE2015-T2-2-059. Numerical computations were carried out at the HPC facilities of the NUS Centre for Advanced 2D Materials, supported by the National Research Foundation of Singapore under its Medium-Sized Centre Programme.

* Corresponding author: vpereira@nus.edu.sg

- [1] J. A. Wilson, *Phys. Status Solidi* **86**, 11 (1978).
- [2] F. Clerc, C. Battaglia, H. Cercellier, C. Monney, H. Berger, L. Despont, M. G. Garnier, and P. Aebi, *J. Phys. Condens. Matter* **19**, 355002 (2007).
- [3] K. Rosnagel, *J. Phys. Condens. Matter* **23**, 213001 (2011).
- [4] A. F. Kusmartseva, B. Sipos, H. Berger, L. Forró, and E. Tutiš, *Phys. Rev. Lett.* **103**, 236401 (2009).
- [5] E. Morosan, H. Zandbergen, B. Dennis, J. Bos, Y. Onose, T. Klimczuk, A. Ramirez, N. Ong, and R. Cava, *Nat. Phys.* **2**, 544 (2006).
- [6] Y. I. Joe, X. M. Chen, P. Ghaemi, K. D. Finkelstein, G. a. de la Peña, Y. Gan, J. C. T. Lee, S. Yuan, J. Geck, G. J. MacDougall, T. C. Chiang, S. L. Cooper, E. Fradkin, and P. Abbamonte, *Nat. Phys.* **10**, 421 (2014).
- [7] P. Chen, Y. H. Chan, X. Y. Fang, Y. Zhang, M. Y. Chou, S. K. Mo, Z. Hussain, a. V. Fedorov, and T. C. Chiang, *Nat. Commun.* **6**, 8943 (2015).
- [8] A. W. Tsen, B. Hunt, Y. D. Kim, Z. J. Yuan, S. Jia, R. J. Cava, J. Hone, P. Kim, C. R. Dean, and A. N. Pasupathy, *Nat. Phys.* **12**, 208 (2015).
- [9] L. J. Li, E. C. T. O’Farrell, K. P. Loh, G. Eda, B. Özyilmaz, and A. H. Castro Neto, *Nature* **529**, 185 (2015).
- [10] X. Xi, Z. Wang, W. Zhao, J.-H. Park, K. T. Law, H. Berger, L. Forró, J. Shan, and K. F. Mak, *Nat. Phys.* **12**, 139 (2015).
- [11] X. Xi, H. Berger, L. Forró, J. Shan, and K. F. Mak, *Phys. Rev. Lett.* **117**, 106801 (2016).
- [12] F. J. Di Salvo, D. E. Moncton, and J. V. Waszczak, *Phys. Rev. B* **14**, 4321 (1976).
- [13] P. Goli, J. Khan, D. Wickramaratne, R. K. Lake, and A. A. Balandin, *Nano Lett.* **12**, 5941 (2012).
- [14] X.-Y. Fang, H. Hong, P. Chen, and T.-C. Chiang, *Phys. Rev. B* **95**, 201409 (2017).
- [15] T. Pillo, J. Hayoz, H. Berger, F. Lévy, L. Schlapbach, and P. Aebi, *Phys. Rev. B* **61**, 16213 (2000).
- [16] D. E. Moncton, J. D. Axe, F. J. Di Salvo, E. Engineers, and E. Engineers, *Phys. Rev. Lett.* **34**, 734 (1975).
- [17] F. Weber, S. Rosenkranz, J.-P. Castellán, R. Osborn, R. Hott, R. Heid, K.-P. Bohnen, T. Egami, A. H. Said, and D. Reznik, *Phys. Rev. Lett.* **107**, 107403 (2011).
- [18] M. Leroux, I. Errea, M. Le Tacon, S.-M. Souliou, G. Garbarino, L. Cario, A. Bosak, F. Mauri, M. Calandra, and P. Rodière, *Phys. Rev. B* **92**, 140303 (2015).
- [19] K. Motizuki, N. Suzuki, Y. Yoshida, and Y. Takaoka, *Solid State Commun.* **40**, 995 (1981).
- [20] M. Calandra and F. Mauri, *Phys. Rev. Lett.* **106**, 196406 (2011).
- [21] B. Singh, C.-H. Hsu, W.-F. Tsai, V. M. Pereira, and H. Lin, *Phys. Rev. B* **95**, 245136 (2017).
- [22] M. Holt, P. Zschack, H. Hong, M. Y. Chou, and T. C. Chiang, *Phys. Rev. Lett.* **86**, 3799 (2001).
- [23] F. Weber, S. Rosenkranz, J. P. Castellán, R. Osborn, G. Karapetrov, R. Hott, R. Heid, K. P. Bohnen, and A. Alatas, *Phys. Rev. Lett.* **107**, 266401 (2011).
- [24] R. Bachrach, M. Skibowski, and F. Brown, *Phys. Rev. Lett.* **37**, 40 (1976).
- [25] A. Zunger and A. J. Freeman, *Phys. Rev. B* **17**, 1839 (1978).
- [26] M. M. Traum, G. Margaritondo, N. V. Smith, J. E. Rowe, and F. J. Di Salvo, *Phys. Rev. B* **17**, 1836 (1978).
- [27] L. V. Keldysh and Y. V. Kopayev, *Sov. Phys.-Solid State, USSR* **6**, 2219 (1965).
- [28] D. Jérôme, T. M. Rice, and W. Kohn, *Phys. Rev.* **158**, 462 (1967).
- [29] W. Kohn, *Phys. Rev. Lett.* **19**, 439 (1967).
- [30] A. Kogar, M. S. Rak, S. Vig, A. A. Husain, F. Flicker, Y. I. Joe, L. Venema, G. J. MacDougall, T. C. Chiang, E. Fradkin, J. van Wezel, and P. Abbamonte, *Science* **358**, 1314 (2017).
- [31] H. Cercellier, C. Monney, F. Clerc, C. Battaglia, L. Despont, M. G. Garnier, H. Beck, P. Aebi, L. Patthey, H. Berger, and L. Forró, *Phys. Rev. Lett.* **99**, 146403 (2007).

- [32] C. Monney, H. Cercellier, F. Clerc, C. Battaglia, E. F. Schwier, C. Didiot, M. G. Garnier, H. Beck, P. Aebi, H. Berger, L. Forró, and L. Patthey, *Phys. Rev. B* **79**, 045116 (2009).
- [33] C. Monney, C. Battaglia, H. Cercellier, P. Aebi, and H. Beck, *Phys. Rev. Lett.* **106**, 106404 (2011).
- [34] G. Monney, C. Monney, B. Hildebrand, P. Aebi, and H. Beck, *Phys. Rev. Lett.* **114**, 086402 (2015).
- [35] J. van Wezel, P. Nahai-Williamson, and S. S. Saxena, *Phys. Rev. B* **81**, 165109 (2010).
- [36] J. van Wezel, P. Nahai-Williamson, and S. S. Saxena, *EPL (Europhysics Letters)* **89**, 47004 (2010).
- [37] P. Chen, Y.-H. Chan, M.-H. Wong, X.-Y. Fang, M. Y. Chou, S.-K. Mo, Z. Hussain, A.-V. Fedorov, and T.-C. Chiang, *Nano Lett.* **16**, 6331 (2016).
- [38] C. Monney, E. F. Schwier, M. G. Garnier, N. Mariotti, C. Didiot, H. Beck, P. Aebi, H. Cercellier, J. Marcus, C. Battaglia, H. Berger, and A. N. Titov, *Phys. Rev. B* **81**, 155104 (2010).
- [39] The fit parameters are: $m_v = 0.63 m_e$, $m_{c,\perp} = 1.38 m_e$, $m_{c,\parallel} = 3.46 m_e$, $\epsilon_{bo} = 0.1$ eV (band overlap). See also supplementary SIII.E.
- [40] Additional details are provided in the supplementary information file which includes references 5, 7, 9, 12, 13, 21, 23, 29–33, 35–37, 43–49, 51–53, 56, 60–69.
- [41] A. Kogar, G. A. de la Pena, S. Lee, Y. Fang, S. X.-L. Sun, D. B. Lioi, G. Karapetrov, K. D. Finkelstein, J. P. C. Ruff, P. Abbamonte, and S. Rosenkranz, *Phys. Rev. Lett.* **118**, 027002 (2017).
- [42] M. Spera, A. Scarfato, E. Giannini, and C. Renner, arXiv (2017), 1710.04096.
- [43] P. Hohenberg and W. Kohn, *Phys. Rev.* **136**, B864 (1964).
- [44] G. Kresse and D. Joubert, *Phys. Rev. B* **59**, 1758 (1999).
- [45] G. Kresse and J. Furthmüller, *Phys. Rev. B* **54**, 11169 (1996).
- [46] J. P. Perdew, K. Burke, and M. Ernzerhof, *Phys. Rev. Lett.* **77**, 3865 (1996).
- [47] S. Baroni, P. Giannozzi, and A. Testa, *Phys. Rev. Lett.* **58**, 1861 (1987).
- [48] A. Togo, F. Oba, and I. Tanaka, *Phys. Rev. B* **78**, 134106 (2008).
- [49] M. Cazzaniga, H. Cercellier, M. Holzmann, C. Monney, P. Aebi, G. Onida, and V. Olevano, *Phys. Rev. B* **85**, 195111 (2012).
- [50] J. F. Zhao, H. W. Ou, G. Wu, B. P. Xie, Y. Zhang, D. W. Shen, J. Wei, L. X. Yang, J. K. Dong, M. Arita, H. Namatame, M. Taniguchi, X. H. Chen, and D. L. Feng, *Phys. Rev. Lett.* **99**, 146401 (2007).
- [51] G. Wu, H. X. Yang, L. Zhao, X. G. Luo, T. Wu, G. Y. Wang, and X. H. Chen, *Phys. Rev. B* **76**, 024513 (2007).
- [52] B. Zenker, H. Fehske, H. Beck, C. Monney, and A. R. Bishop, *Phys. Rev. B* **88**, 075138 (2013).
- [53] G. Grüner, *Density Waves in Solids* (Addison-Wesley, 1994).
- [54] P. Lee, T. Rice, and P. Anderson, *Solid State Commun.* **88**, 1001 (1993).
- [55] W. L. McMillan, *Phys. Rev. B* **16**, 4655 (1977).
- [56] L. Su, C.-H. Hsu, H. Lin, and V. M. Pereira, *Phys. Rev. Lett.* **118**, 257601 (2017).
- [57] V. Olevano, M. Cazzaniga, M. Ferri, L. Caramella, and G. Onida, *Phys. Rev. Lett.* **112**, 049701 (2014).
- [58] M. Calandra and F. Mauri, *Phys. Rev. Lett.* **112**, 049702 (2014).
- [59] M. Hellgren, J. Baima, R. Bianco, M. Calandra, F. Mauri, and L. Wirtz, *Phys. Rev. Lett.* **119**, 176401 (2017).
- [60] H. Bruus and K. Flensberg, *Many-body quantum theory in condensed matter physics: an introduction* (Oxford University Press, 2004).
- [61] C.-W. Chen, J. Choe, and E. Morosan, *Reports Prog. Phys.* **79**, 084505 (2016).
- [62] D. L. Duong, M. Burghard, and J. C. Schön, *Phys. Rev. B* **92**, 245131 (2015).
- [63] H. Frohlich, *Proc. R. Soc. A Math. Phys. Eng. Sci.* **215**, 291 (1952).
- [64] A. V. Krukau, O. A. Vydrov, A. F. Izmaylov, and G. E. Scuseria, *J. Chem. Phys.* **125**, 224106 (2006).
- [65] N. D. Mermin, *Phys. Rev.* **137**, A1441 (1965).
- [66] C. Monney, G. Monney, P. Aebi, and H. Beck, *New Journal of Physics* **14**, 075026 (2012).
- [67] D. Mou, A. Sapkota, H.-H. Kung, V. Krapivin, Y. Wu, A. Kreyssig, X. Zhou, A. I. Goldman, G. Blumberg, R. Flint, and A. Kaminski, *Phys. Rev. Lett.* **116**, 196401 (2016).
- [68] V. Popescu and A. Zunger, *Phys. Rev. B* **85**, 085201 (2012).
- [69] W. D. Wise, M. C. Boyer, K. Chatterjee, T. Kondo, T. Takeuchi, H. Ikuta, Y. Wang, and E. W. Hudson, *Nat. Phys.* **4**, 696 (2008).

— Supplementary Information —

**Reproduction of the charge density wave phase diagram in 1T-TiSe₂ exposes
its excitonic character**

Chuan Chen,^{1,2} Bahadur Singh,^{1,2} Hsin Lin,³ and Vitor M. Pereira^{1,2,*}

¹*Centre for Advanced 2D Materials and Graphene Research Centre,
National University of Singapore, Singapore 117546*

²*Department of Physics, National University of Singapore, Singapore 117542*

³*Institute of Physics, Academia Sinica, Taipei 11529, Taiwan*

(Dated: November 30, 2018)

CONTENTS

| | |
|--|----|
| S-I. The CDW as an excitonic instability | 4 |
| S-I.A. Mean field calculation on the excitonic instability | 4 |
| S-I.B. Stability of CDW phase with doping and temperature | 5 |
| S-I.C. Bare and exciton-renormalized bandstructure | 7 |
| S-I.D. Validity of the single valence band approximation | 8 |
| S-I.E. Mapping chemical potential to doping introduced by Cu intercalation | 10 |
| S-II. Electron-phonon coupling and electron-electron interaction | 12 |
| S-II.A. Mean-field description of the CDW with both excitons and phonons | 12 |
| S-II.B. Estimating the lattice distortion in the excitonic-condensed state | 14 |
| S-III. The lattice instability <i>ab-initio</i> | 14 |
| S-III.A. Details of the DFT calculations | 14 |
| S-III.B. Renormalized band structure: Mexican hat features | 16 |
| S-III.C. GGA and HSE band structure of normal and distorted phase | 17 |
| S-III.D. Unfolded bands with and without doping or distortion | 18 |
| S-III.E. Effective mass from ARPES and DFT calculations | 20 |
| S-III.F. Phonon hardening with Cu doping | 20 |
| S-III.G. Robustness of the PLD and CDW transition with smearing function | 22 |
| S-IV. Pertinence of studying a monolayer for the bulk system | 23 |
| Supplementary References | 26 |

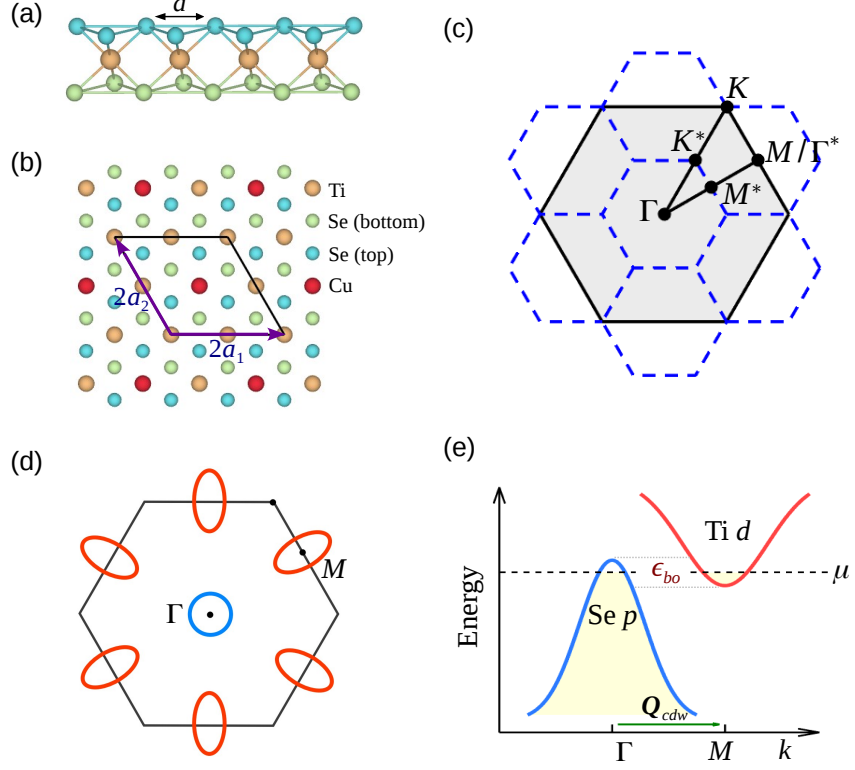


FIG. S1. Crystal structure, Brillouin zone, and bare band topology of the TiSe₂ monolayer. (a) 1T phase with octahedral prismatic local structure of Ti and Se atomic layers. (b) Top view of the TiSe₂ monolayer with Cu doping. The black rhombus identifies the 2×2 supercell and red balls show the Cu atoms which lie above the central Ti atoms in the supercell. \mathbf{a}_1 and \mathbf{a}_2 are the primitive vectors in the normal phase (1×1). (c) BZ of the normal (1×1 , solid black) and distorted (2×2 , dashed blue) phases, where the points marked with * refer to the reduced Brillouin zone. (d) The Fermi contours and (e) schematic band structure near E_F in the normal phase. The Se-derived valence band has its maximum at Γ while the Ti-derived electron pockets are centered at the M points. Their overlap is quantified by ϵ_{bo} and $\Gamma M = \mathbf{Q}_{cdw}$.

S-I. THE CDW AS AN EXCITONIC INSTABILITY

S-I.A. Mean field calculation on the excitonic instability

We formulate the mean field theory using the equation of motion method. The interaction in the Hamiltonian (1) is decoupled in the particle-hole channel as

$$c_{\mathbf{k}+\mathbf{q},\sigma}^\dagger d_{i,\mathbf{k}',\sigma'} = \delta_{\mathbf{k}+\mathbf{q},\mathbf{k}'} \delta_{\sigma,\sigma'} \langle c_{\mathbf{k}',\sigma}^\dagger d_{i,\mathbf{k}',\sigma} \rangle + \left[c_{\mathbf{k}+\mathbf{q},\sigma}^\dagger d_{i,\mathbf{k}',\sigma'} - \delta_{\mathbf{k}+\mathbf{q},\mathbf{k}'} \delta_{\sigma,\sigma'} \langle c_{\mathbf{k}',\sigma}^\dagger d_{i,\mathbf{k}',\sigma} \rangle \right], \quad (\text{S1})$$

$$d_{i,\mathbf{k}'-\mathbf{q},\sigma'}^\dagger c_{\mathbf{k},\sigma} = \delta_{\mathbf{k}+\mathbf{q},\mathbf{k}'} \delta_{\sigma,\sigma'} \langle d_{i,\mathbf{k},\sigma}^\dagger c_{\mathbf{k},\sigma} \rangle + \left[d_{i,\mathbf{k}'-\mathbf{q},\sigma'}^\dagger c_{\mathbf{k},\sigma} - \delta_{\mathbf{k}+\mathbf{q},\mathbf{k}'} \delta_{\sigma,\sigma'} \langle d_{i,\mathbf{k},\sigma}^\dagger c_{\mathbf{k},\sigma} \rangle \right], \quad (\text{S2})$$

so that, by neglecting the product of the fluctuation (bracketed) terms, we achieve the mean-field Hamiltonian

$$H_{\text{MF}} \equiv \sum_{\mathbf{k},\sigma,i} \varepsilon_{v\mathbf{k}} c_{\mathbf{k},\sigma}^\dagger c_{\mathbf{k},\sigma} + \varepsilon_{c\mathbf{k},i} d_{i,\mathbf{k},\sigma}^\dagger d_{i,\mathbf{k},\sigma} - \sum_{\mathbf{k},\sigma,i} \Delta_{i,\mathbf{k},\sigma} c_{\mathbf{k},\sigma}^\dagger d_{i,\mathbf{k},\sigma} - \Delta_{i,\mathbf{k},\sigma}^* d_{i,\mathbf{k},\sigma}^\dagger c_{\mathbf{k},\sigma} + \frac{1}{\mathcal{N}} \sum_{i,\sigma} \sum_{\mathbf{k},\mathbf{k}'} V_{i,\mathbf{k}-\mathbf{k}'} \langle c_{\mathbf{k},\sigma}^\dagger d_{i,\mathbf{k},\sigma} \rangle \langle d_{i,\mathbf{k}',\sigma}^\dagger c_{\mathbf{k}',\sigma} \rangle, \quad (\text{S3})$$

where the order parameter

$$\Delta_{i,\mathbf{k},\sigma} \equiv \frac{1}{\mathcal{N}} \sum_{\mathbf{k}'} V_{i,\mathbf{k}-\mathbf{k}'} \langle d_{i,\mathbf{k}',\sigma}^\dagger c_{\mathbf{k}',\sigma} \rangle \quad (\text{S4})$$

gives a measure of the Fourier component at wavevector \mathbf{Q}_{cdw} of the charge density. In passing, we note the formal analogy between (S3) and (S4), and the equations that describe the SC order parameter in a multi-band s -wave semiconductor within a BCS theory. How the magnitude of V is mentioned in the main text. Also, since all terms in (S3) are spin-diagonal, they will be suppressed in the expressions henceforth, but are implicit in all the results.

The theory is developed in terms of Matsubara Green's functions¹ which requires the definition of normal and anomalous propagators as the τ -ordered thermal averages

$$\mathcal{G}_v(\tau, \mathbf{k}) = -\langle \mathcal{T} c_{\mathbf{k}}(\tau) c_{\mathbf{k}}^\dagger(0) \rangle, \quad (\text{S5a})$$

$$\mathcal{D}_{j,i}(\tau, \mathbf{k}) = -\langle \mathcal{T} d_{j,\mathbf{k}}(\tau) d_{i,\mathbf{k}}^\dagger(0) \rangle, \quad (\text{S5b})$$

$$\mathcal{F}_i(\tau, \mathbf{k}) = -\langle \mathcal{T} d_{i,\mathbf{k}}(\tau) c_{\mathbf{k}}^\dagger(0) \rangle, \quad (\text{S5c})$$

which are straightforwardly seen to obey the following coupled equations of motion (in Matsubara frequency space, $i\omega_n$):

$$(i\omega_n - \varepsilon_{v\mathbf{k}}) \mathcal{G}_v(\omega_n, \mathbf{k}) + \sum_i \Delta_i \mathcal{F}_i(\omega_n, \mathbf{k}) = 1, \quad (\text{S6a})$$

$$(i\omega_n - \varepsilon_{c\mathbf{k},i}) \mathcal{F}_i(\omega_n, \mathbf{k}) + \Delta_i^* \mathcal{G}_v(\omega_n, \mathbf{k}) = 0, \quad (\text{S6b})$$

$$(i\omega_n - \varepsilon_{c\mathbf{k},j}) \mathcal{D}_{j,i}(\omega_n, \mathbf{k}) + \Delta_j^* \mathcal{F}_i^\dagger(\omega_n, \mathbf{k}) = \delta_{j,i}, \quad (\text{S6c})$$

$$(i\omega_n - \varepsilon_{v\mathbf{k}}) \mathcal{F}_i^\dagger(\omega_n, \mathbf{k}) + \sum_j \Delta_j \mathcal{D}_{j,i}(\omega_n, \mathbf{k}) = 0. \quad (\text{S6d})$$

There are 16 coupled equations in the set (S6) because $i, j \in \{1, 2, 3\}$, which are to be solved to obtain the order parameter

$$\Delta_{i,\mathbf{k}} = \frac{k_B T}{\mathcal{N}} \sum_{\mathbf{k}', \omega_n} V_{i,\mathbf{k}-\mathbf{k}'} e^{i\omega_n 0^+} \mathcal{F}_i^\dagger(\omega_n, \mathbf{k}'). \quad (\text{S7})$$

The C_3 symmetry relating the dispersion of the three conduction bands [Fig. S1(d)] and our approximation of dropping the \mathbf{q} -dependence in $V_{i,\mathbf{q}}$ make the order parameter independent of both \mathbf{k} and i , allowing one to set $\Delta \equiv \Delta_{i,\mathbf{k}}$. From equations (S6) one obtains

$$\Delta + \frac{k_B T}{\mathcal{N}} \sum_{\mathbf{k}', \omega_n} \frac{A V \Delta}{|\Delta|^2 B - C} = 0, \quad (\text{S8})$$

with

$$A \equiv (i\omega_n - \varepsilon_{c,2})(i\omega_n - \varepsilon_{c,3}),$$

$$B \equiv (i\omega_n - \varepsilon_{c,2})(i\omega_n - \varepsilon_{c,3}) + (i\omega_n - \varepsilon_{c,1})(i\omega_n - \varepsilon_{c,3}) \\ + (i\omega_n - \varepsilon_{c,1})(i\omega_n - \varepsilon_{c,2}),$$

$$C \equiv (i\omega_n - \varepsilon_{c,1})(i\omega_n - \varepsilon_{c,2})(i\omega_n - \varepsilon_{c,3})(i\omega_n - \varepsilon_v),$$

and all the $\varepsilon_{c,i}$ and ε_v are evaluated at \mathbf{k}' .

It is worth noting that this equation can also be obtained by minimizing the free energy functional $\mathcal{F}[\Delta]$, which is usually formulated within a path-integral formalism. In other words, Eq. (S8) is equivalent to $\partial F[\Delta]/\partial \Delta = 0$, which will be a useful identification below to establish the order of the transition to the excitonic/CDW phase.

S-I.B. Stability of CDW phase with doping and temperature

The degree of band overlap is seen to be quantitatively important but not qualitatively matter in the sense that a small overlap still stabilizes a broken symmetry phase with a sizeable T_c (e.g., when

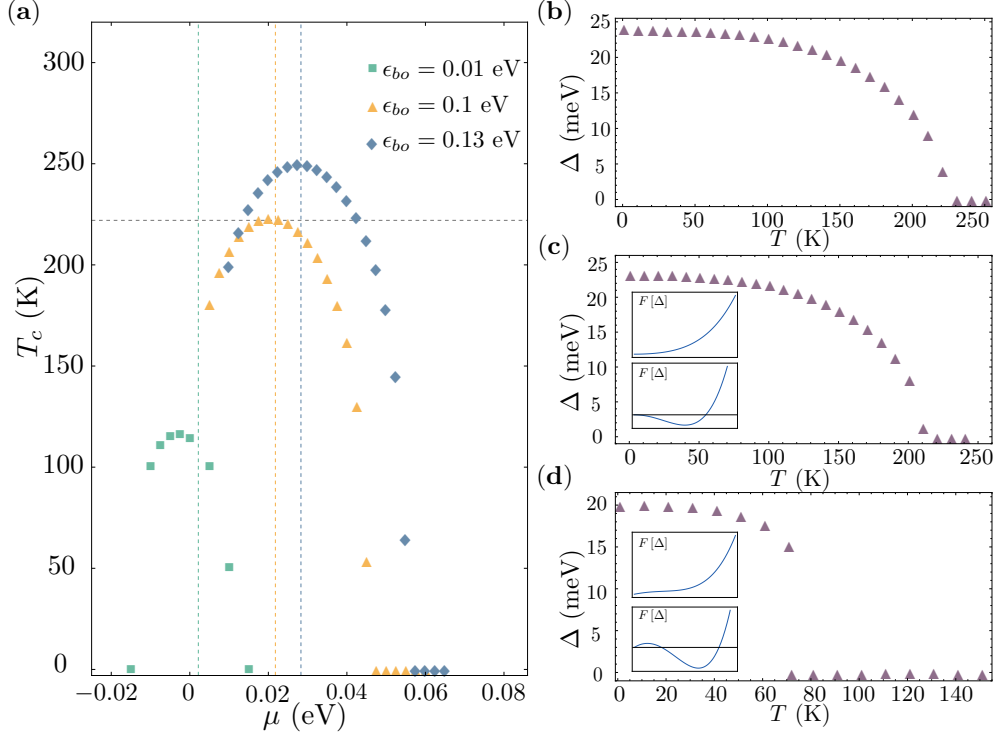


FIG. S2. The CDW phase transition in TiSe₂ according to the excitonic instability alone. (a) Critical temperature (T_c) as a function of chemical potential (μ) for different levels of overlap between the electron and hole pockets, ϵ_{bo} . Zero in the horizontal scale corresponds to μ coinciding with the bottom of conduction pockets. The vertical dashed lines indicate the energies where the bare electron and hole pockets intersect for each case. It is clear that, while small variations in μ tend to quickly reduce T_c , variations in the band overlap have a less significant effect. (b-d) Temperature dependence of the excitonic order parameter, $\Delta(T)$, at different doping: (b) $x = 0$, (c) $x = 0.003$, and (d) $x = 0.042$. The top (bottom) insets in (c) and (d) show the behavior of the free energy as a function of order parameter for $T > T_c$ ($T < T_c$), and illustrate that the transition becomes of first order in our calculation beyond $x \gtrsim 0.038$.

ϵ_{bo} is reduced 10-fold, the optimal T_c is decreased by only 50% to 100 K). Physically, this relative robustness is a sensible outcome because the electronic instability is governed here primarily, not by the number of carriers in each pocket, but by the density of states (DOS) at the point of band intersection in the folded zone. Since the CDW gap opens at that intersection (and not at μ unlike the BCS problem; see supplementary Fig. S3), the CDW phase is most favorable when μ coincides with the band intersection, and progressively weakens when the system is doped in either direction [the intersection energy is signaled by the vertical dashed lines in Fig. S2(a), which correlates with the optimal T_c]. In fact, being such a defining characteristic of the excitonic instability, the existence of an optimum T_c directly correlated with μ at the intersection of the conduction and valence

pockets can provide a clear experimental confirmation of a strong excitonic character associated with the CDW instability. Therefore, experimental confirmation of whether this mechanism is critical or not in driving the CDW instability in TiSe₂ and closely related TMDs can be obtained by probing T_c as a function of both electron and hole doping, to establish: (i) whether or not an optimal T_c exists and (ii) whether it indeed correlates with the pocket intersection. The latter can be identified either by the doping dependence of ARPES spectra or first-principles bandstructure calculations similar to the ones described below. While different pristine systems might have μ naturally above or below the pocket crossing point due to natural doping, the optimal situation should be achievable by deliberate substitution in one direction or the other.

To scrutinize the nature of the phase transition in more detail, we show the temperature dependence of the order parameter in panels (b-d) of Fig. S2. Whereas at low doping we have a clear 2nd order transition [Fig. S2(b,c)], above $x \approx 0.038$ it evolves to 1st order. The insets illustrate schematically the behavior of the corresponding free energy at $T \gtrsim T_c$ and $T \lesssim T_c$. It is physically very significant that this crossover occurs at the densities where ICDW begin to develop experimentally. The fact that the transition becomes of 1st order can be taken as indication of an underlying tendency for phase segregation at $x \gtrsim 0.038$, or that the commensurate state is not the true ground state, one of whose outcomes can certainly be the experimentally observed discommensurations beyond this level of doping². It is noteworthy that our calculation assumes a commensurate CDW from the outset and cannot describe the incommensurate regime. Yet, it predicts its extinction at the doping level where experiments cease to observe a strictly commensurate phase (in other words, the calculation describes both $T_c(x)$ and x_c for the commensurate phase extremely well).

S-I.C. Bare and exciton-renormalized bandstructure

Fig. S3 shows two representative cases of the bare and renormalized bandstructures that result from the self-consistent solution of the excitonic order parameter. The two different band overlaps ($\epsilon_{bo} = 0.1$ eV and $\epsilon_{bo} = 0.01$ eV) were chosen to illustrate the cases of large and small overlap. The dispersion curves are plotted in the reduced (2×2 folded) Brillouin zone as a function of k_y near the folded Γ point. There are always 3 conduction and one valence bands. The chemical potential (μ , dashed gray line at $E = 0$) is set at the value that corresponds to the highest transition temperature for each case (see Fig. S2).

It is worth noting that, whereas at $\epsilon_{bo} = 0.1$ eV the optimal μ defines both electron and hole pockets in the bare bands, for small band overlap ($\epsilon_{bo} = 0.01$ eV) the optimal μ lies slightly below

the bottom of the bare conduction bands and in the gap of the interaction-corrected bandstructure. We remark also the resemblance between the shape of the interaction-corrected bands shown here and the bandstructure obtained by DFT in the relaxed 2×2 distorted phase plotted in Fig. S5.

Perhaps the qualitatively most significant aspect of the CDW transition as seen from the perspective of this excitonic instability is the partial suppression of electronic states below T_c . It is evident in the representative case of Fig. S3(b) that one of the electron pockets is removed with the development of a Mexican hat shaped highest conduction band above μ (inset). This entails a sharp drop in the number of conduction electrons as the temperature decreases through T_c (see also the next section and Fig. S4 below). Simultaneously, the hole pocket disappears as well in the CDW phase, as is clear from the fact that the valence band in Fig. S3(b) (which is shaped like an inverted Mexican hat) is pushed down below the chemical potential. Therefore, according to these results and the physics of the excitonic instability, while in the normal state ($T > T_c$) the transport properties of TiSe_2 are determined by both electrons and holes, when the system enters the CDW state electrons become the majority carriers (holes get suppressed), albeit with an overall smaller electron density on account of the partial loss of electronic states. This is consistent with the well known fact that, experimentally, both Hall effect, Seebeck coefficient, and magnetic susceptibility^{3,4} show a clear transition to electron-like transport as T is lowered below T_c . For example, undoped samples ($x = 0$) of TiSe_2 have a reproducibly positive Hall constant for $T > T_c$, which drops to zero at T_c and becomes steeply negative at $T < T_c$ ^{3,4}. This sharp change in the type and density of the dominant charge carriers is naturally explained by the restructuring of the bands that takes place as a result of the excitonic instability⁵, and further reinforces the key role that this mechanism plays in the CDW transition of TiSe_2 .

S-I.D. Validity of the single valence band approximation

When in the main text we introduced the effective parameterization of the electron and hole pockets for the self-consistent calculation of the excitonic instability, we noted that, although DFT calculations yield two valence bands crossing E_F near the Γ point, in our studies, we modeled the system with only one. This has also been the approach consistently followed in the literature of this system⁵⁻⁷. There are good reasons for such a simplified treatment:

First, the size of the pockets arising from the DFT calculation is strongly sensitive to the functionals and refinements beyond the Local-density approximations. This is not surprising given the extremely reduced carrier density of the system and the known issues with DFT implementations

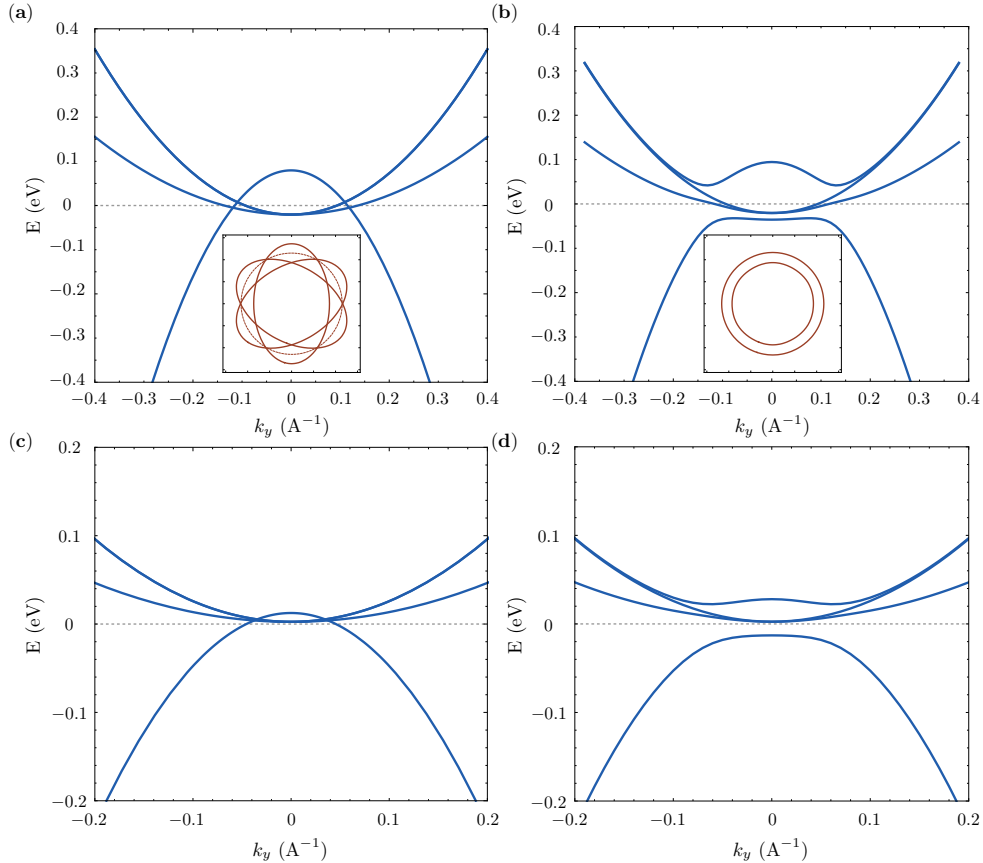


FIG. S3. Bare and renormalized (folded) bandstructure in the excitonic phase. (a) and (b) show, respectively, the bare and the renormalized bands for $\epsilon_{bo} = 0.1$ eV. The insets show the corresponding Fermi surfaces with the dashed circle marking the hole pocket. (c) and (d) show the equivalent representation at $\epsilon_{bo} = 0.01$ eV. The curves are plotted in the reduced Brillouin zone as a function of k_y near the folded Γ point. The chemical potential (μ , dashed gray line at $E = 0$) is set at the value that corresponds to the highest transition temperature for each case (see Fig. 3 in the main text).

capturing band gaps with quantitative accuracy. A reflection of the typical “gap underestimation problem” in our GGA calculation is that the valence bands lie too high in energy, thus leading to large hole pockets. In fact, supplementary supplementary Fig. S6 shows that there is a considerable difference when the calculation is done at the HSE06 level (which counteracts the underestimation): in this case the splitting between the two valence bands is larger and only one hole pocket arises. In addition to this, there is the critical aspect we point out in our discussion and interpretation that the DFT calculation cannot capture the excitonic effects anyway. Therefore, from a DFT point of view it is not clear at the current stage (from our calculations and all those we are aware in the literature) what the accurate “reference” bandstructure is in the normal state, namely whether

there are two or one electron pockets. Hence, there is no basis in using the DFT results of Fig. 3 to conclude that, in order to capture the real situation, one must explicitly include the two valence bands in the mean-field calculation.

Secondly, from the experimental point of view, unfortunately, the situation cannot be unequivocally clarified either because of the extremely small carrier densities that prevent clear access to the conduction bands in ARPES, or because of the above-mentioned fact that CDW/excitonic fluctuations likely cause the system to appear with reconstructed/hybridized bands above the mean-field T_c . Actually, this has been one of the key challenges in settling the nature of the CDW instability in this system because, despite the ability to obtain good-resolution ARPES data, their interpretation has been made in opposing ways through the years in the literature.

Finally, the ARPES data and DFT-HSE calculations reported by Chen et al.⁸ (Fig. 2a in that paper) do show that the separation of the two valence bands is approximately well captured by the HSE calculation (but not their absolute position, which must be rigidly shifted as the authors state, nor the relative position with respect to the conduction bands). This makes it likely that the normal state has only one hole pocket, which would be also consistent with the fact that this second valence band is much less sensitive to temperature, as can be seen in Fig. 3 of the same reference. At any rate, since in the experiments the two bands are distanced by ≈ 0.2 eV, one expects the effect of a putative second pocket, if it exists, to be a correction to the dominant hybridization taking place in the valence band closest to E_F . From the point of view of our mean field calculation, it is not unreasonable to admit that such a correction due to an additional hole pocket could be absorbed in a new value of the interaction parameter of the theory (i.e., in practice treating the two hole pockets as an “effective” single one). For this reason, we do not anticipate different results (neither qualitatively nor quantitatively) if our self-consistent calculation were to be carried out with two hole pockets from the outset.

S-I.E. Mapping chemical potential to doping introduced by Cu intercalation

Our calculations of the excitonic instability are performed at constant chemical potential (μ) which, together with the temperature (T), constitute our externally set thermodynamic parameters. The phase diagram shown in Fig. 1 of the main text is drawn in terms of these two parameters. In order to compare the suppression of critical temperature (T_c) predicted by the excitonic instability with the experimental data available for Cu-intercalated TiSe_2 , the chemical potential was mapped to the Cu content (x) in Cu_xTiSe_2 as follows.

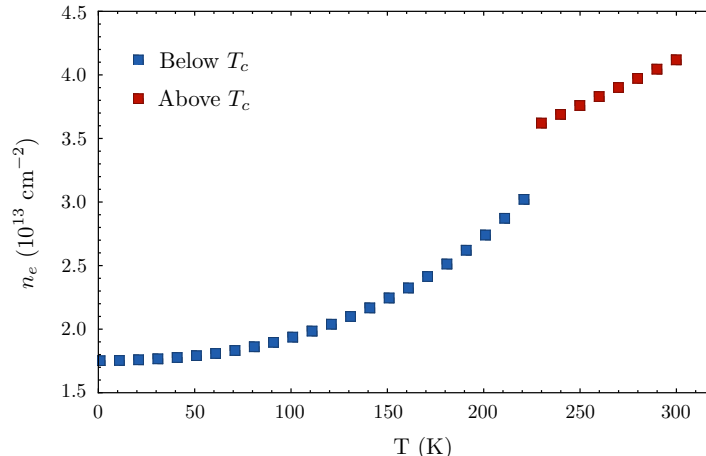


FIG. S4. The electron density above and below T_c at zero doping ($x = 0$). The chemical potential is set as in Fig. S3(a) and we used $\epsilon_{bo} = 0.1$ eV.

Since each Cu atom contributes one additional electron to the system, in Cu_xTiSe_2 there will be x additional electrons in each unit cell. Thus the increase of electronic density would be x/Ω , where Ω stands for the area of the unit cell. When the chemical potential μ is increased with respect to its pristine value (μ_0), the electron (hole) density in the conduction (valence) bands will increase (decrease). Defining $\Delta n_e(\mu) \equiv n_e(\mu) - n_e(\mu_0)$ and $\Delta n_h(\mu) \equiv n_h(\mu) - n_h(\mu_0)$ to denote them separately, charge conservation implies

$$\Delta n_e(\mu) - \Delta n_h(\mu) = x/\Omega, \quad (\text{S9})$$

where the left-hand side of Eq. (S9) can be directly calculated from the electronic band structure.

As an illustration, Fig. S4 shows the electronic density at different temperature and $x = 0$, holding the chemical potential fixed as in Figs. S3(a). The strong drop at T_c is related, primarily, to the partial removal of electron states in the CDW phase and, in addition, to the reconstructed bandstructure whose changes have the most impact for small doping [cf. Fig. S3(b)]. This must have a direct and strong impact in electronic transport by an increase in the resistance. Experimentally, TiSe_2 samples consistently exhibit a characteristic and marked upturn in longitudinal resistivity that accompanies the CDW transition in TiSe_2 . This transport signature has been experimentally observed since the early experiments³ and the sudden increase registered in $\rho(T)$ around T_c is frequently used to track T_c as a function of other experimental parameters^{2,4}. According to the excitonic mechanism, in addition to contributions from scattering by CDW fluctuations in the vicinity of T_c , that signature might be also directly related to the suppression of electronic states as the transition takes place.

S-II. ELECTRON-PHONON COUPLING AND ELECTRON-ELECTRON INTERACTION

In the main text, we have taken into account the electron-electron interaction and studied the excitonic condensation. However, due to the formalism of mean-field theory, one might realize that an same approach to a Hamiltonian with *only* electron-phonon coupling will lead to a same type of gap equation as we had before. In fact, there have been works where both kind of effects were considered^{7,9-11}, however, they are either not fully self-consistent^{7,9} or were done on an simplified (quasi-1D) version of the Hamiltonian^{10,11}. A fully self-consistent study based on the exact Hamiltonian is needed.

In this section, we will show that, even in a system with both electron-electron interaction and electron-phonon coupling, the final form of the gap equation for the charge density order parameter will be similar to the one we have in Eq. (S8).

S-II.A. Mean-field description of the CDW with both excitons and phonons

One should point out that the self-consistent equations that arise from the mean-field decoupling in (S3) and (S4) would be formally equivalent if, instead of through Coulomb interaction, the electron-hole pockets in the original Hamiltonian are coupled by phonons in the way of Fröhlich¹² at \mathbf{Q}_{cdw} . In order to consider both types of interaction, one just needs to add the free phonon part and the electron-phonon coupling to the Hamiltonian we have considered in the main text. A similar type of treatment has also been implemented by B. Zenker et al. in studying the chiral CDW phase¹³. Supposing the electron-phonon coupling is of the form:

$$H_{\text{e-p}} = \frac{1}{\sqrt{N}} \sum_i \sum_{\mathbf{k}, \mathbf{q}} g_{\mathbf{k}, \mathbf{Q}_i + \mathbf{q}} d_{i, \mathbf{k} + \mathbf{q}}^\dagger c_{\mathbf{k}} \left(a_{\mathbf{Q}_i + \mathbf{q}} + a_{-\mathbf{Q}_i - \mathbf{q}}^\dagger \right) + \text{h.c.}, \quad (\text{S10})$$

the mean field Hamiltonian would be of the form

$$H = H_1 + H_2 \quad (\text{S11})$$

$$H_1 = \sum_{\mathbf{q}} \hbar \omega_{\mathbf{q}} a_{\mathbf{q}}^\dagger a_{\mathbf{q}} + \sqrt{\frac{1}{N}} \sum_{i, \mathbf{k}} g_{\mathbf{k}, \mathbf{Q}_i} \left[\langle d_{i, \mathbf{k}}^\dagger c_{\mathbf{k}} \rangle \left(a_{\mathbf{Q}_i} + a_{-\mathbf{Q}_i}^\dagger \right) + \langle c_{\mathbf{k}}^\dagger d_{i, \mathbf{k}} \rangle \left(a_{\mathbf{Q}_i}^\dagger + a_{-\mathbf{Q}_i} \right) \right] \quad (\text{S12})$$

$$H_2 = \sum_{\mathbf{k}, \sigma, i} \varepsilon_{0\mathbf{k}} c_{\mathbf{k}, \sigma}^\dagger c_{\mathbf{k}, \sigma} + \varepsilon_{\mathbf{k}, i} d_{i, \mathbf{k}, \sigma}^\dagger d_{i, \mathbf{k}, \sigma} - \sum_{\mathbf{k}, \sigma, i} (\Delta_{i, \mathbf{k}, \sigma} + \delta_i) c_{\mathbf{k}, \sigma}^\dagger d_{i, \mathbf{k}, \sigma} - (\Delta_{i, \mathbf{k}, \sigma}^* + \delta_i) d_{i, \mathbf{k}, \sigma}^\dagger c_{\mathbf{k}, \sigma}. \quad (\text{S13})$$

Assuming the order parameters are real and do not depend on the direction of the CDW and momentum \mathbf{k} , we have the following expressions for both order parameters:

$$\Delta \equiv \frac{1}{\mathcal{N}} \sum_{\mathbf{k}} V \langle d_{i,\mathbf{k}}^\dagger c_{\mathbf{k}} \rangle, \quad (\text{S14})$$

$$\delta_i = -\frac{1}{\sqrt{\mathcal{N}}} g \langle a_{\mathbf{Q}}^\dagger + a_{-\mathbf{Q}} \rangle = \frac{1}{\mathcal{N}} \frac{g^2}{\omega_{\mathbf{Q}}} \sum_{\mathbf{k}} \left(\langle c_{\mathbf{k}}^\dagger d_{i,\mathbf{k}} \rangle + \langle d_{i,\mathbf{k}}^\dagger c_{\mathbf{k}} \rangle \right) = 2 \frac{g^2}{\omega_{\mathbf{Q}} V} \Delta. \quad (\text{S15})$$

If one compares H_2 and the mean field Hamiltonian in equation (4) of the main text, it can be easily seen that, now, the term $(1 + 2g^2/\omega_{\mathbf{Q}}V) \Delta_i$ plays the role of Δ_i before. It is also important to notice that the *plus* sign here indicates that both interactions collaborate to the CDW transition. One can show that the gap equation for Δ_i is of a similar form to the one discussed in the main text, namely:

$$\Delta + \frac{k_B T}{\mathcal{N}} \sum_{\mathbf{k}, \omega_n} \frac{AV \left(1 + \frac{2g^2}{\omega_{\mathbf{Q}}V}\right) \Delta}{\left(1 + \frac{2g^2}{\omega_{\mathbf{Q}}V}\right)^2 \Delta^2 B - C} = 0, \quad (\text{S16})$$

with the definitions $\alpha = 1 + 2g^2/\omega_{\mathbf{Q}}V$, $V' = \alpha V$ and $\Delta' = \alpha \Delta$. The gap equation above can be recast as

$$\Delta' + \frac{k_B T}{\mathcal{N}} \sum_{\mathbf{k}, \omega_n} \frac{AV' \Delta'}{\Delta'^2 B - C} = 0, \quad (\text{S17})$$

which is exactly the same as equation (9) with the following identifications:

$$V' \leftrightarrow V, \quad \Delta' \leftrightarrow \Delta. \quad (\text{S18})$$

Because of the simple linear relationship between V, Δ and V', Δ' , the solution of Eq. (S17) gives rise to a unique solution for Δ . Correspondingly, the transition temperature is also the same in both cases if V' here is equal to the value of V in the main text.

Consequently, equation (S8) is formally unchanged if one considers both excitons and electron-phonon coupling at $\mathbf{q} = \mathbf{Q}_{\text{cdw}}$ from the outset, in which case V and Δ are reinterpreted in terms of the combined parameters. But, on the one hand, doing so increases the number of parameters in the theory, which might seem unnecessary since it has been previously shown that, if the excitonic mechanism alone can capture the experimental temperature dependence, the lattice responds with a PLD in agreement with experiments⁷. On the other hand, one anticipates a dominant effect of the electronic interactions because of the very small carrier densities. This suggests that, despite the fact that both phonons and excitons will necessarily be coupled and soften together, one should

assign a strong excitonic character to this instability. Finally, a full self-consistent treatment of both mechanisms would always be limited by the inability of accurately describing the phonon spectrum as a function of temperature. Instead, we corroborate the importance of interactions by determining the predictions that follow in their absence using unbiased, state of the art DFT computations of the phonon instabilities and bandstructures of TiSe_2 with doping. Since these, predominantly accounting for the electron-phonon coupling, fail to accurately describe the doping dependence, we conclude that the relative contribution of the excitons to the mean field phase diagram cannot be small, and is likely to be dominant.

S-II.B. Estimating the lattice distortion in the excitonic-condensed state

Monney *et al.* have recently shown that, given a finite order parameter $\Delta(T)$ whose temperature dependence follows the experiments, combining the exciton condensate with electron-phonon coupling leads to a PLD with correct order of magnitude in the lattice displacement of undoped TiSe_2 ⁷. Although their calculation is not self-consistent and only establishes how the lattice softens in response to the exciton condensate, the result does reinforce the strong influence that the excitonic instability can have in the stability of the lattice.

Furthermore, incorporating our self-consistent calculation of Δ in the (T, x) parameter space (Fig. S2) into such calculations, provides a complete picture of the CDW/PLD in TiSe_2 with electronic and lattice degrees of freedom. This would not be surprising in itself because electronic interactions are known to be sufficient to stabilize robust CDW phases even in the absence of a PLD, particularly in reduced dimensions¹⁴⁻¹⁸. However, it would be incorrect to consider phonons as simple spectators because, on the one hand, self-consistency involving both electron-electron and electron-phonon interaction is expected to further stabilize the PLD; on the other hand, the latest experimental evidence shows that this system carries hybrid electronic and lattice elementary excitations close to T_c ¹⁹.

S-III. THE LATTICE INSTABILITY *AB-INITIO*

S-III.A. Details of the DFT calculations

Our *ab initio* calculations were done within the DFT framework²⁰ with the projector augmented wave method implemented in the Vienna Ab-initio Simulation Package (VASP)^{21,22}. Except when stated otherwise, we resort to the generalized gradient approximation (GGA)²³ for the exchange-

correlation functional and include spin-orbit coupling. To simulate the normal and distorted TiSe₂ monolayers, a thick vacuum slab of more than 12 Å is used to prevent interaction between the periodically repeated images. The BZ was sampled with a Γ -centered $16 \times 16 \times 1$ \mathbf{k} -mesh and a plane wave basis set with energy cut-off of 380 eV. The in-plane lattice constant and atomic positions were relaxed until residual forces became less than 1 meV/Å. Force constants were obtained within density functional perturbation theory (DFPT) and the phonon dispersions computed with the PHONOPY code^{24,25}.

Ground-state electronic and vibrational properties are calculated with a small smearing parameter ($\sigma = 0.01$ eV). Technically, this is a parameter to accelerate convergence without direct physical meaning; it acquires the physical meaning of electronic temperature only when used in conjunction with finite temperature smearing methods^{26–28}. We discuss results obtained with different smearing strategies in one of the supplementary sections further down.

In order to facilitate a direct comparison of calculated energy spectra with the available ARPES results, we perform the unfolding of the supercell band structure to the primitive cell BZ. The essence of this procedure is to find a plane wave in the supercell BZ associated with a primitive cell's k -point. This is done by projecting the supercell wavefunctions onto primitive cell and calculating spectral weights as discussed in references 28 and 29.

The effects of additional carriers in TiSe₂ were investigated with two complementary strategies. First, we explicitly studied the doping induced by Cu by simulating supercells with adsorbed Cu. Subsequently, for the systematic study of the phonon instabilities, electron (hole) doping was considered by adding (removing) electrons to the unit cell, with a neutralizing uniform background charge.

The internal atomic positions in the unit cell were relaxed for each doping while keeping the lattice parameter fixed at its undoped value. For the study of Cu-intercalated TiSe₂, Cu atoms were placed directly above and below the central Ti in a 2×2 supercell [see Figs. S1 (a)-(b)]. All the atoms were allowed to freely relax inside the unit cell. Interestingly, despite unconstrained, the Cu atoms adsorb onto the surface without bouncing back into the vacuum with an adsorption energy of $E_{ads} = 2.456$ eV/Cu, where $E_{ads} = -[E_{rel}(\text{Cu}_x\text{TiSe}_2) - E_{rel}(\text{TiSe}_2) - E(\text{Cu})]$. The structural stability of these Cu-adsorbed TiSe₂ monolayers was further scrutinized by calculating the phonon spectrum.

To track the evolution of σ_c with electron density, we calculated the phonon spectrum covering a range of different σ for each doping. Fig. S9(a) shows the representative case of $x = 0.04$ where the imaginary frequencies disappear if $\sigma > 0.4$ eV. As this threshold smearing is very similar to that

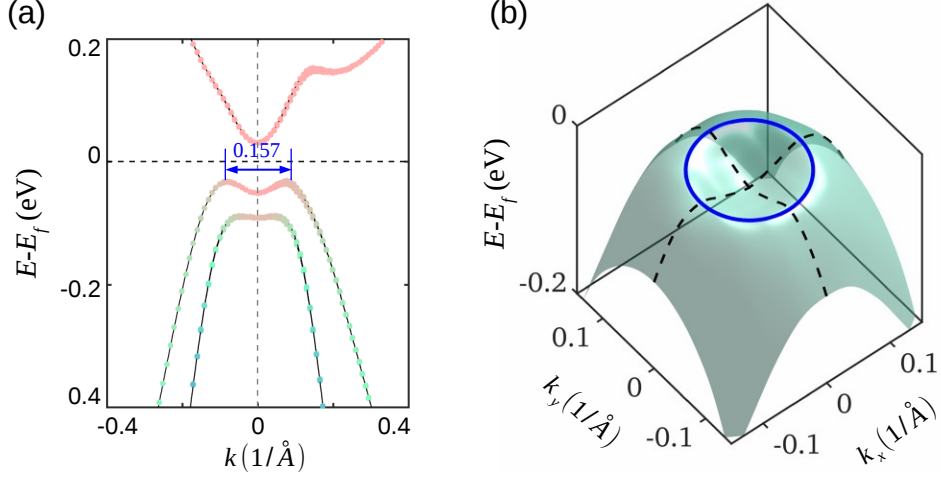


FIG. S5. (a) Electronic band structure of undoped TiSe_2 monolayers with the PLD. (b) Zoom-in structure of top valence band in the $E - k_x - k_y$ space within the reduced Brillouin zone. Black dashed lines show the band structure along two orthogonal directions and blue ring highlights the valence band maximum in the reduced Brillouin zone.

of the undoped monolayer, it would suggest that the CDW/PLD phase is as robust at this doping as in pristine form, unlike the experimental situation!

S-III.B. Renormalized band structure: Mexican hat features

In Fig. S5 we show a close-up of the restructured bands in undoped TiSe_2 , whose ground state we determine to be the 2×2 PLD with wavevector \mathbf{Q}_{cdw} after full relaxation of the ions in the unit cell [see also Fig. 3 in the main text]. The top valence bands are seen to lose their $-k^2$ parabolic dispersion and develop the shape of an inverted Mexican hat. More specifically, the top of the valence band moves from $k = 0 \text{ \AA}^{-1}$ to lie at $k = 0.0785 \text{ \AA}^{-1}$. A 3D rendition of this band shows that the maximum defines a circle of diameter 0.157 \AA^{-1} centered at $k = 0$, as marked by the blue circle in Fig. S5. This is additionally supported by the fact that the energy dispersion along two orthogonal directions flattens exactly on this circle. Both perspectives establish the inverted Mexican hat shape of the band dispersion in the distorted phase (ground state). As discussed earlier by Kohn³⁰ and emphasized by Cazzaniga *et al.* with DFT+GW calculations for bulk TiSe_2 ³¹, this shape is typical of the excitonic phases.

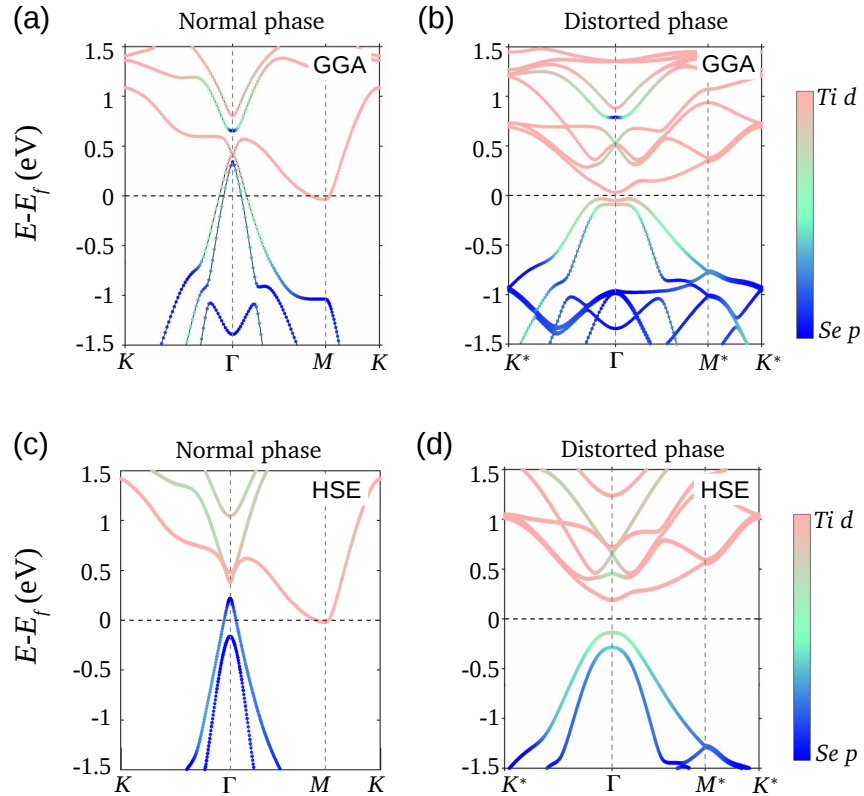


FIG. S6. Electronic band structure of the (a,c) normal and (b,d) distorted phase of undoped TiSe_2 calculated with GGA (top row) and HSE (bottom row). The semimetal nature of the normal phase and the gapped state of the distorted one remain robust with these functionals.

S-III.C. GGA and HSE band structure of normal and distorted phase

Local and semi-local GGA functionals normally underestimate the orbital occupations. The more advanced HSE exchange-correlation functional uses a part of exact Fock exchange and is known to correct the orbital occupations, yielding results in closer agreement with experimental band structures. We computed the band structure of the normal and distorted phases using the GGA and the HSE06³² hybrid.

In Fig. S6, we compare the band structures of the normal and distorted phases of monolayer TiSe_2 obtained with these two energy functionals [the GGA band structures shown in Figs. S6(a)-(b) are also presented in the main text in Figs. 3(a) and 3(c)]. As discussed in the main text, the normal phase GGA band structure has a semimetal character with a clear energy overlap between the valence and conduction states. The HSE band structure, on the other hand, shows a rigid shift of the valence and conduction states with a decrease in the band overlap, Fig. S6(c), but still retaining the semimetal character in the normal phase.

In the distorted phase, the HSE band structure shown in Fig. S6(d) retains the overall features of the bands in the GGA, including the semiconducting (gapped) state. However, the hybridization of the valence and conduction bands leads to an energy gap of 325 meV which considerably overestimates (by 172 meV) the experimentally reported value of $\simeq 153$ meV (at 10 K)^{8,28}. By comparison, the GGA gap is $E_g = 82$ meV, which underestimates the experimental value by 71 meV. An underestimation of the calculated gap is generically expected in the absence of quasiparticle (GW) corrections. In addition, the inverted Mexican hat profile of the valence states is nearly suppressed in the HSE result: the diameter of the Mexican hat is much smaller than in the GGA (Fig. S5) to the extent that, while it is clearly visible in Fig. S6(b), it is not resolved in the equivalent plot of Fig. S6(d).

The larger deviation (and overestimation) of the band gap and the near suppression of the band restructuring near E_F within HSE, justifies our choice of using the GGA to compute the band structure of both electrons and phonons in this problem.

S-III.D. Unfolded bands with and without doping or distortion

In Fig. S7 we reproduce the band structures shown in Fig. 3 of the main text. As described there, these were obtained using a 2×2 unit cell. Panel (a) shows the resulting dispersion when the ions are held in place; it simply corresponds to the band structure of the normal (undistorted) phase in the reduced Brillouin zone identified by the dashed honeycomb in Fig. S1(c). Panel (b) shows the electronic spectral function of the same bands unfolded back to the original (1×1) Brillouin zone, where one sees the familiar hole pocket at Γ and the electron pocket(s) at M .

Fig. S7(c) shows the band structure generated when the ions are allowed to relax freely within the 2×2 unit cell: The system reaches the ground state by creating a lattice distortion which, simultaneously, reshapes the bands near E_F as discussed earlier and lowers the total energy. The corresponding spectral function in the unfolded zone is plotted in panel (d). In contrast with (b), we now see spectral weight that duplicates the hole dispersion originally near Γ around M , and electron dispersion originally around M gets shadowed around Γ . This agrees with ARPES measurements in both bulk⁶ and monolayer samples⁸.

Fig. S7(f) shows the unfolded spectral function associated with the bands in panel (e). It illustrates that, just as doping has little effect in the band structure near the pocket intersection, doping has also a mild effect in the shadowing of spectral weight. Note that, as explained in the main text, the band structures shown in (e,f) have been obtained with two relaxed Cu atoms in the

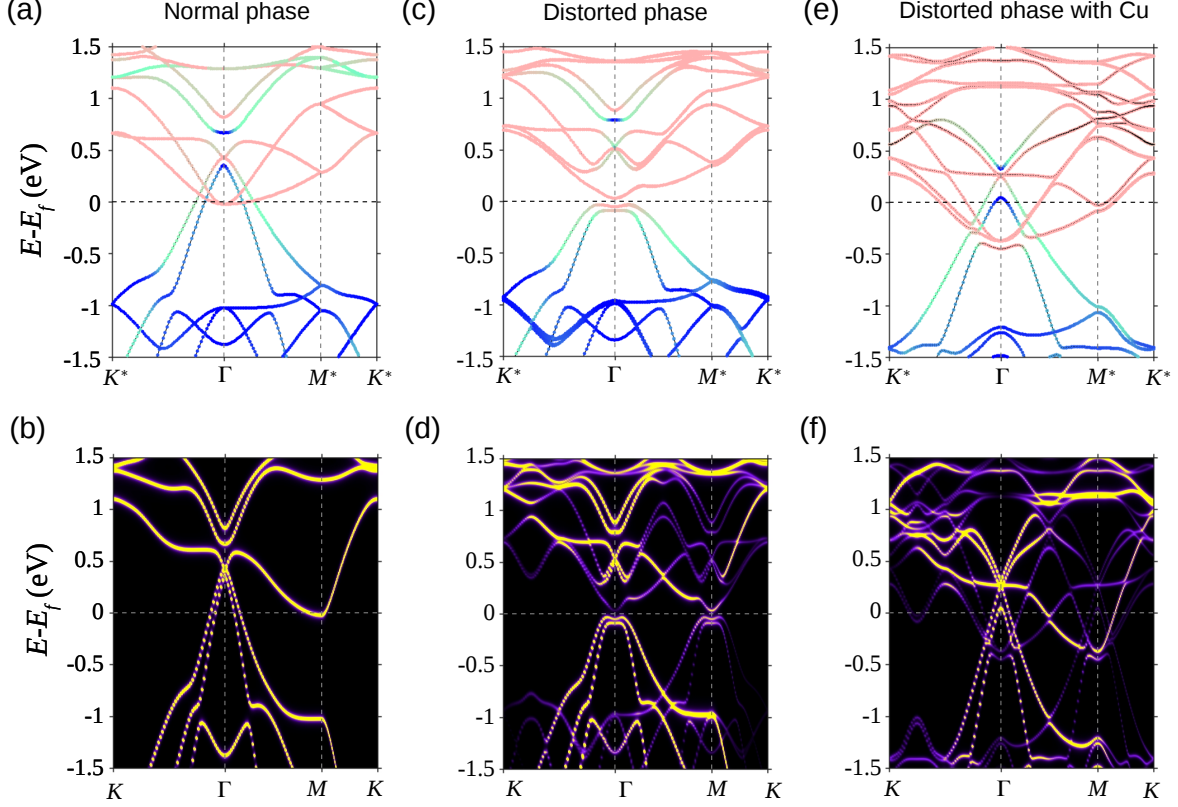


FIG. S7. Effect of the PLD and Cu doping on the electronic structure of TiSe_2 . Shown are the band structure in the unrelaxed, normal phase (a,b), in the relaxed distorted phase (c,d), and in the relaxed phase with Cu doping (e,f). Each column plots the bands in the 2×2 reduced Brillouin zone of the distorted phase (top) and the corresponding unfolded version in the BZ of the undistorted phase (bottom). The bands obtained without lattice relaxation in (a) have the Ti-derived electron pocket folded into the Γ point without any restructuring or gap opening; they are restored back to the M point in the unfolded representation (b). The situation is quite different when the lattice is allowed to relax on a 2×2 supercell: in addition to the spontaneous lattice distortion, we observe a finite band gap and the appearance of two back-folded bands at the M point (c,d). Adsorbed Cu atoms electronically dope the system and raise the Fermi level higher in the conduction bands without noticeable disruption to the overall dispersion (e,f) in comparison with the undoped case (c,d).

2×2 unit cell, thus corresponding to a Cu:Ti ratio of 50%. This is extremely high, in comparison with the experimental solubility limit of 11%^{4,33}. Yet, the main effect is electron doping without significant qualitative change in the energy band dispersion.

S-III.E. Effective mass from ARPES and DFT calculations

As described in the main text, our calculations of the excitonic instability rely entirely on the bandstructure parameters obtained from ARPES in the normal state, which are stated in footnote/reference [39] of the manuscript. The effective masses, in particular, are $m_{c,\parallel} = 3.46m_e$, $m_{c,\perp} = 1.38m_e$, $m_v = 0.63m_e$. From our DFT GGA calculation we obtain $m_{c,\parallel} = 3.46m_e$ and $m_{c,\perp} = 0.22m_e$. On the other hand, the relevant valence band obtained from DFT deviates quickly from a quadratic dispersion (hyperbolic like); the best approximation to a quadratic dispersion yields about $m_{\text{DFT}}^v \sim 0.19m_e$.

As far as the CDW instability is concerned, the most relevant comparison is expected to be for the effective masses along the direction of \mathbf{Q}_{cdw} (i.e., the m_{\parallel}). In the conduction band, the ARPES-derived and DFT-calculated m_{\parallel} match well. The mass associated with the (isotropic) valence band is however off by a factor of about 3. But, even though one could suggest that, by predicting the valence electrons to be too light, DFT is missing effects of quasiparticle mass renormalization due to interactions that are either missed or incompletely taken into account, such statement cannot generally be put on solid ground: on the one hand, the GGA framework always treats the correlation problem in an effective way, preventing a direct quantitative assessment of these effects; on the other hand, such comparison is looking at the effective masses in the normal/undistorted phase which is not the true ground state of the lattice. In other words, we can conceive a situation in which, despite moderate interactions, the band parameters for the true ground state are in acceptable agreement, but forcing a DFT bandstructure calculation in the 1×1 state might yield a large discrepancy in comparison with the experimental spectral function obtained in the normal state.

S-III.F. Phonon hardening with Cu doping

As discussed in the main text as well in our earlier work²⁸, the low-temperature state of an undoped TiSe_2 monolayer is the CDW phase with an accompanying PLD. Our DFT and DFPT calculations demonstrate that Cu adsorption (which corresponds to intercalation in bulk systems) suppresses the PLD and eventually stabilizes a 1×1 undistorted structure at zero temperature. In the main text, this transition as a function of doping is established by studying the density beyond which the dynamical phonon instability disappears at $T = 0$ (cf. Fig. 4); as explained and justified there, these calculations are done by adding additional electrons to the unit cell.

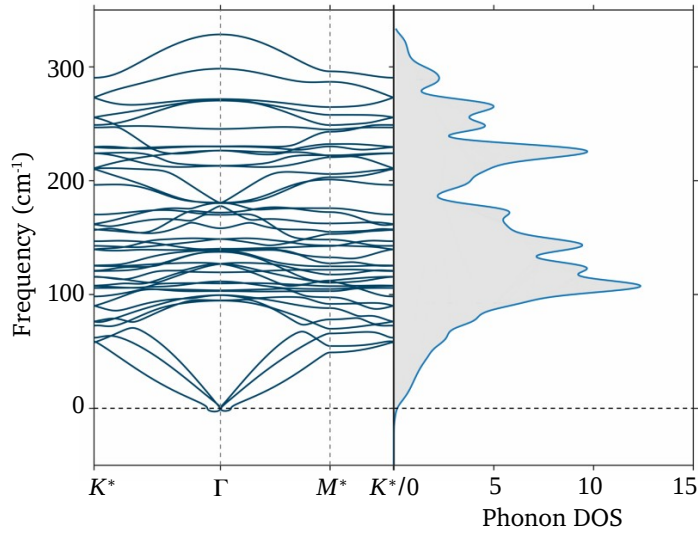


FIG. S8. Phonon band dispersion (left) and phonon density of states (right) of a Cu-doped 2×2 TiSe₂ monolayer at low smearing parameter. The absence of imaginary frequencies in the reduced Brillouin zone confirms the dynamical stability in the presence of the Cu adsorbates.

Here, we wish to demonstrate that this conclusion holds when the phonon spectrum is computed including the Cu atoms explicitly in the unit cell from the outset. Fig. S8 summarizes the phonon spectrum and corresponding density of states obtained under such conditions, with two Cu atoms per 2×2 supercell (one adsorbed above and the other symmetrically below the TiSe₂ monolayer, as in Fig. S1(b)). We highlight that this phonon spectrum has been calculated using the same structure that is employed to determine the band structure shown in Fig. 3(c) of the main text. Fig. S8 does not show any imaginary frequencies nor soft acoustic branch, thereby confirming the dynamical stability of the Cu doped monolayer at low temperature. This small simulation cell corresponds to a 50% Cu content ($x=0.5$), it tallies with the evolution of σ_c shown in Figs. 1 and 4 (main text) based on the electron doping approach that predicts the lattice to be stable for $x \gtrsim 0.20$. It also reinforces the validity of the latter approach for numerical expediency in treating the experimentally relevant doping levels of $0 < x < 11$ which, to explore with actual Cu atoms in the supercell, would require extremely large supercells, prohibitive for both the DFT electronic structure and DFPT phonon calculations.

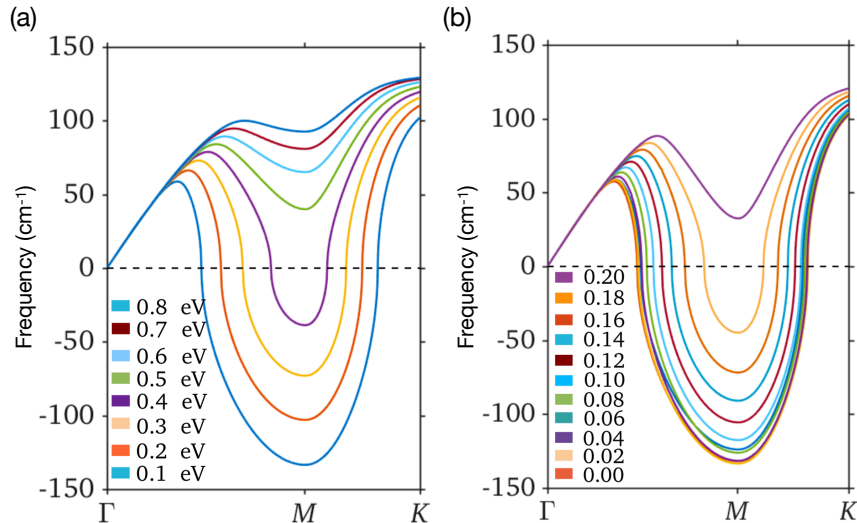


FIG. S9. Calculated phonon modes and the suppression of the PLD in the TiSe₂ monolayer with temperature and doping. (a) The soft mode along the relevant high-symmetry directions for different σ (see legends) and fixed doping of $x = 0.04$ electrons per formula unit (e/fu). (b) Same as (a) but for different electronic doping at fixed $\sigma = 0.01$ eV. Legends show x in e/fu.

S-III.G. Robustness of the PLD and CDW transition with smearing function

In electronic structure calculations, the smearing function is routinely used to decide how to set the partial occupancies for each wavefunction. For a particular smearing method, σ determines the width of smearing. An optimal choice for smearing function and σ depends not only on improved convergence but also on the system and properties of interest. However, all methods should converge to the ground state in the limit $\sigma \rightarrow 0$.

In order to verify the robustness of our conclusions regarding the evolution of the dynamical phonon instability and PLD with doping, we calculated the phonon dispersions of undoped TiSe₂ using two independent strategies: the Methfessel-Paxton (MP) smearing and Fermi-Dirac (FD) smearing methods. The resulting phonon spectra at different σ are shown in Fig. S10. It is evident that both approaches correctly predict the freezing of the longitudinal acoustic mode at the experimentally correct \mathbf{Q}_{cdw} , and the existence of a threshold σ_c above which this instability is suppressed. Note, however, that the magnitude of σ_c varies for different smearing strategies, and reflects the fact that σ is not the physical temperature, and should only be used to explain qualitative trends in the lattice structure as a function of temperature. These results are consistent with earlier calculations done for bulk TiSe₂²⁷.

One of our central conclusions in the main text is that relying only on the phonons calculated

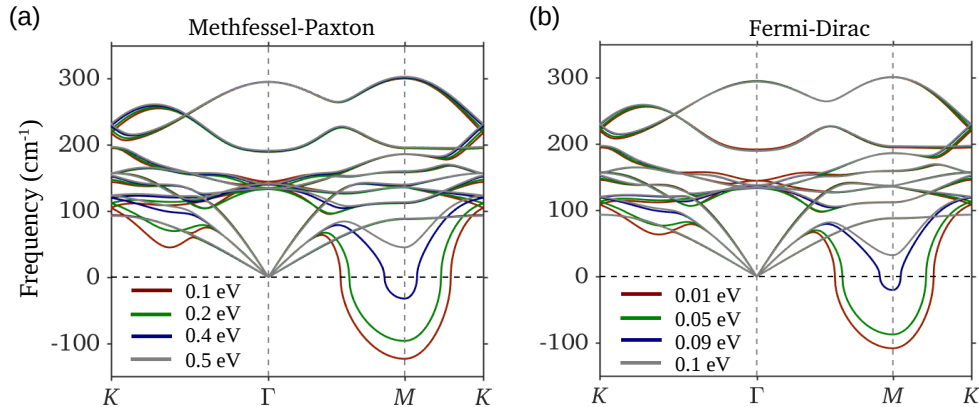


FIG. S10. Phonon dispersion of the 1×1 TiSe_2 monolayer (normal phase) calculated with different smearing parameter (σ) using: (a) Methfessel-Paxton smearing and (b) Fermi-Dirac smearing. Imaginary frequencies are represented as negative values.

within DFT+DFPT to predict the critical doping (x_c) above which the CDW/PLD is no longer stable, leads us to values of x_c that overshoot the experimental threshold by about one order of magnitude. Crucially, this result is also independent of the smearing method used, as we show in Fig. S11: both MP and FD smearing predict the PLD to remain as the ground state at least up to $x = 0.16$. Conversely, this implies, by extrapolation, that $x_c \gtrsim 0.20$ if x_c is extracted from the criterion $\sigma_c(x) = 0$.

Seeing that there is complete consistency among the calculated phonon dispersion and phonon instabilities with these two smearing methods, we chose to present in the main text the results obtained with the Methfessel-Paxton smearing because of its improved convergence and accuracy over Fermi-Dirac smearing.

It is important to remark, though, that the actual relation between σ and T depends on the smearing strategy used. In addition, the physical temperature includes contributions not only from the electrons but also from the phonons. However, although this means that σ_c cannot be directly related to T_c , existence of a finite σ_c can be safely used to predict a finite T_c .

S-IV. PERTINENCE OF STUDYING A MONOLAYER FOR THE BULK SYSTEM

We studied the monolayer TiSe_2 in the mean field calculation and compared the results with existing experiments on bulk systems. As a matter of principle, quantum confinement effects can lead to quantitative and/or qualitative differences in the electronic band structures of monolayer and bulk TiSe_2 . However, as discussed in various previous studies, as well as reported in recent

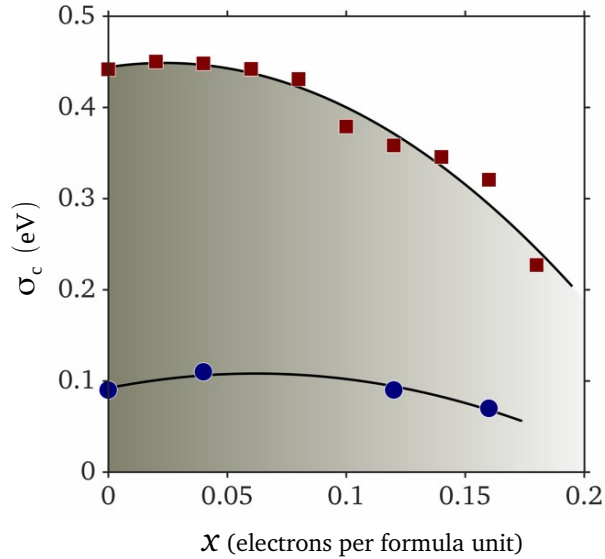


FIG. S11. The critical smearing parameter (σ_c) as a function of doping x according to the two different smearing strategies discussed in the text. The values of σ_c are obtained from studying the phonon spectrum for different σ as in Fig. S10. All phonon frequencies are real (no dynamical instability) for $\sigma > \sigma_c$. The red points were obtained with Metthfessel-Paxton and the blue using Fermi-Dirac smearing (black lines are guides). Note how, despite having different magnitudes (see text), the two strategies agree in the qualitative prediction that the phonon instability persists up to very large values of x .

experiments, the CDW transition in both monolayer and bulk TiSe_2 involves the interplay of states that lie within a narrow energy of E_F . These states are represented by the Se p -derived top portion of the highest valence band and Ti d -derived bottom portion of the lowest conduction band. Other bands located elsewhere in the Brillouin zone near the Fermi level are insensitive to the atomic distortion associated with the CDW transition and do not contribute significantly to the energetics and stability of the CDW in either bulk or monolayer TiSe_2 ^{5,8,28,31}.

The observed experimental spectral function in the normal and CDW phases of the monolayer clearly resembles the spectral function of the bulk. Furthermore, it has been established experimentally that the evolution of the CDW phase with carrier density, as well as the onset and shape of the superconducting dome, is qualitatively and quantitatively similar in atomically-thin films and bulk samples^{2,4}. This clearly indicates that the CDW physics in monolayer TiSe_2 is similar to that of the bulk, and that intra-layer electronic and phononic processes are clearly dominant in determining the phase transitions. This, of course, is not surprising given the strongly two-dimensional character (both structurally and electronically) of the bulk crystal, imposed by the vertical stacking of weakly coupled TiSe_2 monolayers.

It should be noted that despite decades of experimental and theoretical studies on bulk TiSe_2 , the CDW physics in this system remains controversial. Obvious reasons involve the 3D nature of the CDW order in bulk crystals, which challenges the identification of the exact gap locations and weight transfer in the 3D Brillouin zone. As demonstrated by recent experiments on monolayer^{8,34} and thin films^{2,35}, individual layers of TiSe_2 undergo a 2×2 transition at temperatures close to those of the bulk T_c (slightly higher due to reduced screening, see below), with density modulation of wavevector $\mathbf{Q}_{\text{cdw}} = \Gamma M$. This $\mathbf{Q}_{\text{cdw}} = \Gamma M$ in the monolayer system corresponds precisely to the projection of the three-dimensional wavevector (ΓL) onto the horizontal plane³. The difference between the charge-density profile in individual layers and bulk is that, in the latter, the Van der Waals stacking in the third dimension causes neighboring layers to lock their individual 2×2 structures into a $2 \times 2 \times 2$ anti-phase modulation to further minimize the electrostatic interaction across layers¹⁴. This results in the overall 3D CDW order observed in neutron or X-ray scattering, for example^{3,36}. Therefore, these experiments establish that the critical aspect of this problem is that *the CDW transition is driven by the action taking place within each layer*; the additional three-dimensional modulation is a somewhat minor consequence of the vertical stacking of individual 2×2 CDWs.

Consequently, a detailed study of the 2D CDW and its evolution with doping can clarify the connection between the 2D bulk order and help in provide long-sought answers related to the physics underlying the CDW instability in TiSe_2 , bulk or monolayer. In addition, the reduced screening implies that electrons and holes in the 2D case are more strongly coupled with each other than in the 3D counterpart according to the excitonic mechanism where electron-electron interactions play a crucial role. Therefore, the 2D excitonic phase is expected to be more stable than in the 3D counterpart. This prediction (or feature) from the excitonic physics is entirely in line with the experimental observation that T_c systematically increases with decreasing sample thickness^{8,35}.

In conclusion, since all recent experimental information concurs in that the CDW order is stabilized by the intra-layer physics, and the phase diagram is qualitatively the same as a function of doping, and quantitatively differs only in the fact that thinner samples have slightly higher T_c , the theoretical study of an isolated monolayer is sufficient to characterize the key microscopic details at play, even in bulk TiSe_2 .

* Corresponding author: vpereira@nus.edu.sg

- ¹ H. Bruus and K. Flensberg, *Many-body quantum theory in condensed matter physics: an introduction* (Oxford University Press, 2004).
- ² L. J. Li, E. C. T. O'Farrell, K. P. Loh, G. Eda, B. Özyilmaz, and A. H. Castro Neto, *Nature* **529**, 185 (2015).
- ³ F. J. Di Salvo, D. E. Moncton, and J. V. Waszczak, *Phys. Rev. B* **14**, 4321 (1976).
- ⁴ E. Morosan, H. Zandbergen, B. Dennis, J. Bos, Y. Onose, T. Klimczuk, A. Ramirez, N. Ong, and R. Cava, *Nat. Phys.* **2**, 544 (2006).
- ⁵ C. Monney, H. Cercellier, F. Clerc, C. Battaglia, E. F. Schwier, C. Didiot, M. G. Garnier, H. Beck, P. Aebi, H. Berger, L. Forró, and L. Patthey, *Phys. Rev. B* **79**, 045116 (2009).
- ⁶ H. Cercellier, C. Monney, F. Clerc, C. Battaglia, L. Despont, M. G. Garnier, H. Beck, P. Aebi, L. Patthey, H. Berger, and L. Forró, *Phys. Rev. Lett.* **99**, 146403 (2007).
- ⁷ C. Monney, C. Battaglia, H. Cercellier, P. Aebi, and H. Beck, *Phys. Rev. Lett.* **106**, 106404 (2011).
- ⁸ P. Chen, Y. H. Chan, X. Y. Fang, Y. Zhang, M. Y. Chou, S. K. Mo, Z. Hussain, a. V. Fedorov, and T. C. Chiang, *Nat. Commun.* **6**, 8943 (2015).
- ⁹ C. Monney, G. Monney, P. Aebi, and H. Beck, *New Journal of Physics* **14**, 075026 (2012).
- ¹⁰ J. van Wezel, P. Nahai-Williamson, and S. S. Saxena, *Phys. Rev. B* **81**, 165109 (2010).
- ¹¹ J. van Wezel, P. Nahai-Williamson, and S. S. Saxena, *EPL (Europhysics Letters)* **89**, 47004 (2010).
- ¹² H. Frohlich, *Proc. R. Soc. A Math. Phys. Eng. Sci.* **215**, 291 (1952).
- ¹³ B. Zenker, H. Fehske, H. Beck, C. Monney, and A. R. Bishop, *Phys. Rev. B* **88**, 075138 (2013).
- ¹⁴ G. Grüner, *Density Waves in Solids* (Addison-Wesley, 1994).
- ¹⁵ W. D. Wise, M. C. Boyer, K. Chatterjee, T. Kondo, T. Takeuchi, H. Ikuta, Y. Wang, and E. W. Hudson, *Nat. Phys.* **4**, 696 (2008).
- ¹⁶ D. Mou, A. Sapkota, H.-H. Kung, V. Krapivin, Y. Wu, A. Kreyssig, X. Zhou, A. I. Goldman, G. Blumberg, R. Flint, and A. Kaminski, *Phys. Rev. Lett.* **116**, 196401 (2016).
- ¹⁷ L. Su, C.-H. Hsu, H. Lin, and V. M. Pereira, *Phys. Rev. Lett.* **118**, 257601 (2017).
- ¹⁸ C.-W. Chen, J. Choe, and E. Morosan, *Reports Prog. Phys.* **79**, 084505 (2016).
- ¹⁹ A. Kogar, M. S. Rak, S. Vig, A. A. Husain, F. Flicker, Y. I. Joe, L. Venema, G. J. MacDougall, T. C. Chiang, E. Fradkin, J. van Wezel, and P. Abbamonte, *Science* **358**, 1314 (2017).
- ²⁰ P. Hohenberg and W. Kohn, *Phys. Rev.* **136**, B864 (1964).
- ²¹ G. Kresse and D. Joubert, *Phys. Rev. B* **59**, 1758 (1999).
- ²² G. Kresse and J. Furthmüller, *Phys. Rev. B* **54**, 11169 (1996).
- ²³ J. P. Perdew, K. Burke, and M. Ernzerhof, *Phys. Rev. Lett.* **77**, 3865 (1996).
- ²⁴ S. Baroni, P. Giannozzi, and A. Testa, *Phys. Rev. Lett.* **58**, 1861 (1987).
- ²⁵ A. Togo, F. Oba, and I. Tanaka, *Phys. Rev. B* **78**, 134106 (2008).

- ²⁶ N. D. Mermin, *Phys. Rev.* **137**, A1441 (1965).
- ²⁷ D. L. Duong, M. Burghard, and J. C. Schön, *Phys. Rev. B* **92**, 245131 (2015).
- ²⁸ B. Singh, C.-H. Hsu, W.-F. Tsai, V. M. Pereira, and H. Lin, *Phys. Rev. B* **95**, 245136 (2017).
- ²⁹ V. Popescu and A. Zunger, *Phys. Rev. B* **85**, 085201 (2012).
- ³⁰ W. Kohn, *Phys. Rev. Lett.* **19**, 439 (1967).
- ³¹ M. Cazzaniga, H. Cercellier, M. Holzmann, C. Monney, P. Aebi, G. Onida, and V. Olevano, *Phys. Rev. B* **85**, 195111 (2012).
- ³² A. V. Krukau, O. A. Vydrov, A. F. Izmaylov, and G. E. Scuseria, *J. Chem. Phys.* **125**, 224106 (2006).
- ³³ G. Wu, H. X. Yang, L. Zhao, X. G. Luo, T. Wu, G. Y. Wang, and X. H. Chen, *Phys. Rev. B* **76**, 024513 (2007).
- ³⁴ P. Chen, Y.-H. Chan, M.-H. Wong, X.-Y. Fang, M. Y. Chou, S.-K. Mo, Z. Hussain, A.-V. Fedorov, and T.-C. Chiang, *Nano Lett.* **16**, 6331 (2016).
- ³⁵ P. Goli, J. Khan, D. Wickramaratne, R. K. Lake, and A. A. Balandin, *Nano Lett.* **12**, 5941 (2012).
- ³⁶ F. Weber, S. Rosenkranz, J. P. Castellán, R. Osborn, G. Karapetrov, R. Hott, R. Heid, K. P. Bohnen, and A. Alatas, *Phys. Rev. Lett.* **107**, 266401 (2011).